Dynein-2 is required for a functional transition zone and bidirectional ciliary trafficking

Laura Vuolo[1], Nicola L. Stevenson[1], Kate J. Heesom[2], David J. Stephens[1]

[1] Cell Biology Laboratories, School of Biochemistry, University of Bristol, Bristol, UK.

[2] Proteomics Facility, Faculty of Biomedical Sciences, University of Bristol, Bristol, UK.

SHORT TITLE: Dynein-2 subunit knockouts define its roles in ciliogenesis

Number of characters: 38322

SUMMARY: Here, Vuolo and colleagues use engineered knockout human cell lines to define roles for dynein-2 intermediate chains. WDR34 is required for axoneme extension, while WDR60 is not. Both subunits are required for cilia transition zone organization and bidirectional intraflagellar transport.

Abstract

The dynein-2 microtubule motor functions as the retrograde motor for intraflagellar transport and is required for the formation and maintenance of primary cilia. Mutations in dynein-2 components cause skeletal ciliopathies, notably Jeune syndrome. Dynein-2 comprises a heterodimer of two non-identical intermediate chains, WDR34 and WDR60. Here, we use knockout cell lines to demonstrate that each intermediate chain has a distinct role in cilia function. Both proteins are required to maintain a functional transition zone and for efficient bidirectional intraflagellar transport, only WDR34 is essential for axoneme extension. In contrast, only WDR60 is essential for co-assembly of the other subunits. Furthermore, WDR60 cannot compensate for loss of WDR34 or vice versa. This work defines a functional asymmetry to match the subunit asymmetry within the dynein-2 motor. Analysis of causative point mutations in WDR34 and WDR60 can partially restore function to knockout cells. Our data show that Jeune syndrome is caused by defects in transition zone architecture as well as intraflagellar transport.

Introduction

Cytoplasmic dyneins are minus-end directed motors that use the energy of ATP hydrolysis to move along microtubules. Two cytoplasmic dyneins have been identified. The better-characterized dynein-1 is involved in the transport of cargos in the cytoplasm, organelle dynamics and in mitotic spindle organization during mitosis (Roberts et al., 2013). Dynein-2 is responsible for retrograde transport in cilia and flagella. Primary (non-motile) cilia are hair-like extensions present on almost all animal cells that act as antennae for extracellular signals and are fundamental to proper metazoan development and ongoing health. They integrate signals in key pathways including sonic hedgehog (Shh), Wnt and platelet-derived growth factor signaling and participate in metabolic control and autophagy (Reiter and Leroux, 2017). Cilia are particularly important to ensure correct Shh signaling during embryonic development (Goetz and Anderson, 2010; He et al., 2017). Defects in cilia are linked to many human diseases, known collectively as ciliopathies, including developmental disorders, neurodegeneration and metabolic diseases (Reiter and Leroux, 2017; Yee and Reiter, 2015).

Ciliogenesis is initiated in non-dividing cells by the docking of pre-ciliary vesicles with the mother centriole. The pre-ciliary vesicles fuse and then surround the mother centriole concomitant with the assembly of a series of protein modules that form a diffusion barrier separating the distal end of the mother centriole from the rest of the cell cytoplasm (Garcia-Gonzalo et al., 2011). A microtubule bundle, the axoneme, then extends from the centriole to allow cargo transport by the process of intraflagellar transport (IFT) (Yee and Reiter, 2015). A “transition zone” (TZ) that separates the mother centriole from the main length of the axoneme forms a diffusion barrier for both soluble and membrane proteins at the base of the cilium (Garcia-Gonzalo et al., 2011; Garcia-Gonzalo and Reiter, 2017). Once established, cilia are maintained and operated by the process of IFT (Hou and Witman, 2015). IFT-B complexes (comprising of a core subcomplex, including nine subunits (IFT88, -81, -74, -70, -52, -46, -27, -25, and -22) with five additional, peripherally-associated subunits (IFT172, -80, -57, -54, and -20)) undergo kinesin-2-driven motility from base to tip where the complexes are then reorganized prior to retrograde transport of IFT-A (comprising 6 subunits (IFT144, IFT140, IFT139, IFT122, IFT121/WDR35, and IFT43)) driven by dynein-2 (Hou and Witman, 2015; Jensen and Leroux, 2017). This process ensures the correct localization of receptors and signaling molecules within cilia as well as act in signal transduction from the cilium to the rest of the cell.

The genes encoding subunits of the dynein-1 and dynein-2 motors are largely distinct. Some light chain subunits are common to both but the major subunits (heavy, intermediate and light intermediate chains) are different between the two holoenzyme complexes. Dynein-2 is built around a heavy chain dimer of DYNC2H1 (DHC2) (Criswell et al., 1996; Mikami et al., 2002). This associates

with two intermediate chains, WDR34 and WDR60, first identified as dynein-2 subunits named FAP133 and FAP163 in *Chlamydomonas* (Patel-King et al., 2013; Rompolas et al., 2007) and subsequently shown to be components of metazoan dynein-2 (Asante et al., 2013; Asante et al., 2014). This asymmetry distinguishes dynein-2 from dynein-1 where two identical IC subunits form the holoenzyme. The reason for this asymmetry is unclear. In addition, a dynein-2-specific light intermediate chain (DYNC2LI1/LIC3) has been identified (Hou and Witman, 2015; Mikami et al., 2002) as well as a specific light chain, TCTEX1D2 (Asante et al., 2014; Schmidts et al., 2015). Mutations in genes encoding dynein-2 subunits are associated with skeletal ciliopathies, notably short rib-polydactyly syndromes (SRPSs) and Jeune asphyxiating thoracic dystrophy (JATD, Jeune syndrome). These are recessively inherited developmental disorders characterized by short ribs, shortened tubular bones, polydactyly and multisystem organ defect (Huber and Cormier-Daire, 2012). In recent years, whole exome-sequencing technology has enabled the identification of new mutations involved in skeletal ciliopathies, notably a range of mutations affecting dynein-2 heavy chain (DYNC2H1 or DHC2, (Chen et al., 2016; Cossu et al., 2016; Dagoneau et al., 2009; El Hokayem et al., 2012; Mei et al., 2015; Merrill et al., 2009; Okamoto et al., 2015; Schmidts et al., 2013a)). Additionally, mutations in WDR34 (Huber et al., 2013; Schmidts et al., 2013b), WDR60 (Cossu et al., 2016; McInerney-Leo et al., 2013), LIC3 (Kessler et al., 2015; Taylor et al., 2015) and TCTEX1D2 (Schmidts et al., 2015) have also been reported. The role of dynein-2 heavy chain has been extensively studied in *Chlamydomonas*, *C. elegans,* and mice. In all cases, loss of dynein heavy chain results, in short, stumpy cilia that accumulate IFT particles at the tip, consistent with a role of dynein-2 in retrograde ciliary transport (Hou and Witman, 2015). Recently, more interest has been focused on the role of the subunits associated with DHC2. Two studies in *Chlamydomonas* and in human patient-derived fibroblasts revealed that LIC3 (D1bLIC in *Chlamydomonas*) plays an important role for ciliogenesis and stability of the entire dynein-2 complex (Li et al., 2015; Taylor et al., 2015). Similarly, loss of Tctex2b (TCTEX1D2) destabilizes dynein-2 and reduces IFT in *Chlamydomonas* (Schmidts et al., 2015).

Previous work from our lab and others has shown that loss of function of dynein-2 intermediate chains, WDR34 and WDR60, is associated with defects in cilia. Knockdown of WDR60 or WDR34 in hTERT-RPE1 cells results in a reduction of ciliated cells, with an increase or decrease of the cilia length, likely depending on depletion efficiency (Asante et al., 2014). Mutations in WDR34 have also been shown to result in short cilia with a bulbous ciliary tip in patients fibroblast cells affected by SRP (Huber et al., 2013). Consistent with the results obtained in patient cells, loss of WDR34 in mice also results in short and stumpy cilia with an abnormal accumulation of ciliary proteins and defects in Shh signaling (Wu et al., 2017). Similarly, mutations in WDR60 patient fibroblasts are associated

with a reduction in cilia number, although the percentage of ciliated cells was variable in different affected individuals (McInerney-Leo et al., 2013). These findings are all consistent with roles for WDR34 and WDR60 in IFT.

In this study, we sought to better understand the role of dynein-2 in human cells using engineered knockout (KO) cell lines for WDR34 and WDR60. We define a functional asymmetry within the complex, where WDR34 is absolutely required for ciliogenesis, while WDR60 is not. In contrast, WDR60 is essential to maintain the integrity of the ciliary transition zone and for retrograde trafficking of IFT particles. Furthermore, by expressing HA-tagged WDR34 in WDR60 KO cells and HA-tagged WDR60 in WDR34 KO cells, we found that WDR34 is not required for the other subunits to assemble, whereas loss of WDR60 leads to significant defects in dynein-2 holocomplex assembly. We propose a model where dynein-2 requires WDR34 for axoneme extension but not for the assembly of the other subunits of the complex, whereas WDR60 is crucial for dynein-2 stability, IFT, and ciliary transition zone assembly and/or maintenance. Analysis of disease-causing patient mutations further defines the role of dynein-2 in cilia formation and function.

112 ## Results

113 *WDR34 or WDR60 play different roles in cilia function*

114 To understand the function of WDR34 and WDR60, we generated KO human telomerase-
115 immortalized RPE1 (hTERT-RPE1) cells using CRISPR-Cas9. We derived two WDR34 KO clones (1 and
116 2) using guide RNAs (gRNAs) targeting exons 2 and 3, and one KO clone for WDR60, targeting exon 3.
117 Genomic sequencing of these clones identified insertion/deletion mutations on the targeted
118 sequences (Fig. S1). All cell clones were analyzed for protein expression by immunoblot using
119 polyclonal antibodies. Neither WDR34 nor WDR60 was detected in the respective KO cells compared
120 to the controls (Fig. S2A and Fig. S2B) which provides evidence that downstream initiation sites are
121 not being used. To mitigate against the possibility of any off-target effects, we grew KO cells
122 alongside control CRISPR cells which had been transfected and treated the same way as the KO, but
123 genomic sequencing showed no mutation at the target site. These cells (WDR34 KO CTRL and
124 WDR60 KO CTRL) did not present any cilia defects when stained with Arl13b or IFT88 (Fig. S2C and
125 S2D). Images in all figures show WT cells where indicated. Indistinguishable results were obtained
126 using these control cell lines. Defects in ciliogenesis in both WDR34 and WDR60 KO cells were
127 rescued by overexpressing WT proteins, confirming that the phenotypes we observed were not due
128 to off-target mutations (described below).

129 Loss of WDR34 severely impaired the ability of these cells to extend a microtubule axoneme (Fig. 1A,
130 B), although Arl13b localized within those few cilia that did form. In contrast, loss of WDR60 did not
131 significantly affect the ability of cells to extend an axoneme (Fig. 1B). Cilia were shorter in both
132 WDR60 and WDR34 KO cells (Fig. 1C). Next, we examined the assembly and structure of primary cilia
133 in WDR34 and WDR60 KO cells by transmission electron microscopy (EM). After 24 hr of serum
134 starvation, WT RPE1 cells extend a defined axoneme surrounded by a ciliary membrane (Fig. 1D). In
135 contrast, WDR34 KO cells failed to extend an axoneme (Fig. 1E) but showed a large docked pre-
136 ciliary vesicle, consistent with the small Arl13b-positive structures seen by immunofluorescence.
137 WDR60 KO cells showed apparently normal cilia (Fig. 1F) with normal basal body structures and
138 axoneme extension. However, when an entire cilium was captured in WDR60 KO serial sections (Fig.
139 1G), we observed a bulged cilia tip containing accumulated electron dense particles (Fig. 1H). To our
140 surprise, we also observed the ciliary membrane bulged at a second point along the axoneme and
141 this region contained intraciliary vesicular structures (Fig. 1Hi).

142 *Loss of WDR34 and WDR60 causes accumulation of proteins at the ciliary tip*

143 The abnormal structure of cilia in the KO cells led us to analyze the steady-state localization of the
144 IFT machinery. After 24 hr serum starvation, IFT88 (part of IFT-B) was found almost exclusively at the

145 base of the cilia in wild-type (WT) RPE1 cells (Fig. 2A, quantified in Fig. 2Ai), but in WDR60 KO and
146 WDR34 KO cells IFT88 was found throughout the cilia and accumulated at the tip (Fig. 2A, 2Aii, and
147 2Aiii). Similarly, another IFT-B component, IFT57 (Fig. 2B) was enriched at the cilia tips in WDR60 and
148 WDR34 KO cells. Quantification of the localization of these IFT-B proteins showed an accumulation
149 of both IFT88 (Fig. 2C) and IFT57 (Fig. 2D) at both the base and tip of the cilia in WDR60 KO cells. In
150 WDR34 KO cells, IFT-B proteins were seen to accumulate at the tip of cilia. The accumulation at the
151 base seen in WDR60 KO cells was not evident in WDR34 KO cells. The limited numbers of ciliated
152 WDR34 KO cells precluded further quantification. Another IFT-B protein, IFT20 (Fig. 2E), was
153 enriched at both the tip and the base of cilia in WDR60 KO cells (quantification in Fig. 2F). IFT20 is
154 the only IFT component found to localize to the Golgi until now. As expected, IFT20-GFP was found
155 at the Golgi in WT cells, although the Golgi pool of IFT20-GFP seen in WT cells was largely absent
156 from WDR60 KO cells (Fig. 2G).

157 Next, we analyzed the localization of IFT-A proteins. We found that both IFT140 (Fig. 3A) and IFT43
158 (Fig. 3B) were accumulated along the length of the axoneme within cilia in WDR60 KO cells, as well
159 as at the tips in the few cilia present in WDR34 KO cells, while they were found only at the base of
160 the cilia in WT cells (quantification in Fig. 3Ai-iii and 3Bi-iii). Further quantification showed that both
161 IFT140 (Fig. 3C) and IFT43 (Fig. 3D) are accumulated in WDR60 KO cilia compared to controls. Both
162 IFT140 and IFT43 show a more pronounced accumulation at ciliary tips in WDR34 KO cells. In
163 addition, we determined the localization of a subunit of the anterograde kinesin-2 motor, KAP3
164 which was also accumulated at the ciliary tip of WDR60 KO (Fig. 3E).

165 To study whether defects in dynein-2 affect the transport of membrane proteins we used GFP-
166 fusions with Arl13b, somatostatin receptor type 3 (SSTR3), 5-hydroxytryptamine receptor type 6
167 (5HT6) and Rab8a. We found that in live cells Arl13b-GFP and EGFP-SSTR3 accumulate at the ciliary
168 tip (Fig. 4A and 4B). Surprisingly, we also noticed a consistent reduction in the amount of Arl13b-GFP
169 within cilia in WDR60 KO cells (Fig. 4C and 4Ci). The same observation was made with EGFP-SSTR3
170 (Fig. 4D and 4Di) and EGFP-5HT6 (Fig. 4E and 4Ei). In contrast, GFP-Rab8a localization in the cilia was
171 indistinguishable between WT and WDR60 KO cells (Fig 4F and 4Fi).

172 *Dynein-2 is required for ciliary transition zone assembly*

173 Previous studies have shown that the protein content of cilia is maintained by a diffusion barrier
174 formed by the transition zone. Changes in transition zone composition have been associated with
175 the mislocalization of ciliary proteins, including the membrane marker Arl13b (Li et al., 2015; Shi et
176 al., 2017). To test if the reduction in Arl13b seen in our WDR60 KO was caused by a defect in the
177 transition zone, we labeled KO and WT cilia with known transition zone markers. We found that the

178 core transition zone marker, RPGRIP1L (also known as MKS5), is no longer restricted to an area
179 adjacent to the mother centriole in WDR60 KO cells (Fig. 5A, quantified in 5Ai). Conversely, TMEM67
180 (also known as MKS3), which in WT cilia extends from the basal body through a more distal region,
181 becomes much more tightly restricted to the base of the cilium in WDR60 KO cells (Fig. 5B,
182 quantified in 5Bi). We also determined the transition zone organization in WDR34 KO cells. The few
183 cilia found in the WDR34 KO cells recapitulate the same phenotype observed in the WDR60 KO cilia
184 with an expansion of RPGRIP1L to a more distal position and a reduction of the TMEM67 domain
185 (Fig. 5A and Fig. 5B). In contrast to TMEM67 and RPGRIP1L, no changes were observed for the
186 transition zone marker TCTN1 in both WDR34 KO and WDR60 KO cells with respect to the control
187 (Fig. 5C).

188 *Unregulated entry of Smoothened into cilia following loss of WDR60*

189 Defects in the dynein-2 motor have been previously associated with deregulation of the Shh
190 pathway (May et al., 2005). Smoothened (Smo), a key component of Shh signaling, localizes to the
191 cilia in response to Shh stimulation but is normally excluded from cilia in cells that have not been
192 treated with Shh or an equivalent agonist such as Smoothened agonist (SAG). Unexpectedly, we
193 found that Smo was localized to cilia in WDR60 KO cells even in the absence of SAG stimulation (Fig.
194 6A, and 6Ai). This localization did not increase upon agonist treatment. In contrast, Smo was indeed
195 excluded from cilia in WT cells at steady state (Fig. 6A and 6Ai) but was readily detected within cilia
196 following SAG stimulation (Fig. 6B, 6Bi, and 6Bii).

197 *Expression of wild-type and patient mutants of WDR60 and WDR34 in KO cells*

198 Many mutations in WDR34 and WDR60 have been associated with SRPs and JATD syndromes. We
199 engineered selected patient mutations into WDR34 and WDR60 to determine the defect compared
200 to expression of wild-type proteins. Two WDR60 mutations were selected from one SRPS patient
201 with compound heterozygosity for WDR60 (WDR60[T749M], WDR60[Q631*]) and two WDR34
202 mutations from two patients with JATD syndromes (WDR34[A22V], WDR34[C148F]). The first
203 WDR60 mutation is located in the third WD repeat (WDR60[T749M]) and the second
204 (WDR60[Q631*]) is located just before the WD repeat domain (Fig. S3A). We undertook “rescue”
205 experiments in which we stably expressed WT or mutant versions of WDR34 and WDR60 in KO cells.
206 Protein expression of stably transfected WT and HA-WDR60 mutants in WDR60 KO cells is shown in
207 Fig. 7A. Both WT HA-WDR60 and HA-WDR60[T749M] efficiently rescued defects in the localization of
208 IFT88 (Fig. 7B). However, expression of HA-WDR60[Q631*] was unable to restore the basal body
209 localization of IFT88 (Fig. 7B and 7Bi). Similar data were obtained for the localization of IFT140 (Fig.
210 7C and 7Ci); expression of both WT and the HA-WDR60[T749M] mutant of WDR60 restored the

211 localization of IFT140 to the base of the cilia, but in cells expressing HA-WDR60[Q631*], IFT140 was
212 found throughout the cilium, as it was in WDR60 KO cells. Next, we tried to mimic the compound
213 heterozygosity occurring in patient cells, generating a stable cell line that expresses both WDR60
214 [T749M] and [Q631*] mutants. When the two mutants were co-expressed in the same WDR60 KO
215 cells we saw no additive effects or dominant negative effects, but cilia appeared normal with IFT88
216 only localized to the base (Fig. S3B, S3C) as was seen with the HA-WDR60[T749M] mutant.

217 In parallel, we also analyzed the phenotype of WDR34 KO cells stably expressing WT and mutant
218 forms of WDR34. We found that expression of WT mGFP-WDR34 restored ciliogenesis and axoneme
219 extension in WDR34 KO cells and that, unexpectedly, this was also true of cells expressing WDR34
220 incorporating either [A22V] or [C148F] mutations (Fig. 7D and 7Di). These disease-causing mutations
221 were chosen as they lie in regions without specific domain prediction. The cilia that formed in
222 WDR34 KO cells expressing either mGFP-WDR34[A22V] or mGFP-WDR34[C148F] were also positive
223 for Arl13b (Fig. 7D). Moreover, WT and both WDR34 mutants were able to rescue IFT88 localization
224 to the basal body (Fig. 7E).

225 To better understand the function of WDR60 we analyzed how the complex is assembled by
226 performing immunoprecipitation of WT and mutant WDR60 proteins. We found that
227 immunoprecipitation of HA-WDR60 expressed in WDR60 KO cells effectively pulls down the
228 chaperone NudCD3, known to interact with dynein-2 via its WD repeat domains. As expected,
229 NudCD3 did not bind to HA-WDR60[Q631*] lacking the WD repeat domain. WT WDR60 also bound
230 effectively to WDR34 and, notably, this interaction was very similar with the HA-WDR60[T749M] or
231 [Q631*] mutants (Fig. 8A). In contrast, LIC3 is readily detected with WT WDR60 but less so with
232 WDR60[T749M]; only a very small amount of LIC3 was detected bound to WDR60[Q631*] (Fig. 8B).
233 TCTEX1 was found to bind effectively to both WT and HA-WDR60[T749M] but less well to HA-
234 WDR60[Q631*] (Fig. 8B). Next, we tested the interactions with IFT proteins, the primary cargo of the
235 ciliary motors. We found that WT WDR60 can bind to IFT140, IFT88, and IFT57; WDR60[T749M]
236 binds to all 3 IFT subunits tested but binds less well to IFT140 (Fig. 8C). In contrast, WDR60[Q631*]
237 pulled down reduced levels of IFT88 and IFT57 and did not interact with IFT140.

238 *The stability of dynein-2 complex in WDR34 and WDR60 KO cells*

239 It has been reported that loss of some components of dynein-2 modifies the stability of the whole
240 dynein-2 complex. In *Chlamydomonas* depletion or loss of LIC3 (D1bIC2) causes a reduction of DHC2
241 in whole cells lysate, whereas the expression level of the intermediate chain is less affected (Reck et
242 al., 2016). Similar results were obtained analyzing expression levels of DHC2 in patients cells with
243 LIC3 mutations (Taylor et al., 2015). We have shown previously that siRNA depletion of WDR34

244 affects the stability of WDR60 and vice versa (Asante et al., 2014). To determine whether loss of one
245 intermediate chain had an effect on the stability of the other, we analyzed levels of WDR34 and
246 WDR60 in whole cells lysate of KO cells. Notably, we found that expression levels of WDR34 were
247 reduced in WDR60 KO cells, although not completely lost. Correspondingly, there was a reduction of
248 WDR60 expression levels in WDR34 KO whole cell lysate (Fig. 9A). Next, we sought to determine the
249 effect of WDR60 and WDR34 loss on the localization of other dynein-2 subunits. We found that LIC3
250 (DYNC2LI1) localized in cilia of WT cells, but this localization was lost in WDR34 or WDR60 cells (Fig.
251 9B). DHC2 was detected at the base of the cilia in WT and WDR60 KO cells, but not along the cilia
252 axoneme. Interestingly, DHC2 localization at the ciliary base was reduced in WDR34 KO cells (Fig.
253 9C). Moreover, we found that TCTEX1 (DYNC1LT1, Fig. 9D) was enriched at the base of the cilium in
254 WT cells, with no changes in WDR34 or WDR60 KO cells. To test how the loss of one dynein-2
255 intermediate chain affected the localization of the other we overexpressed HA-WDR34 and HA-
256 WDR60 in WDR60 and WDR34 KO cells. Both HA-WDR34 and HA-WDR60 were enriched at the base
257 and in the cilia axoneme in WT cells (Fig. S4A and Fig. S4B). We observed no changes in the
258 localization of HA-WDR34 in WDR60 KO cells, which was detected at the base and in the cilia (Fig.
259 S4B). Surprisingly, HA-WDR60 was greatly enriched in stumpy cilia of WDR34 KO cells compared to
260 the cilia in WT cells (Fig. S4A). Overexpression of HA-WDR60 could not rescue axoneme elongation in
261 WDR34 KO cells (Fig. S4C). Additionally, overexpression of HA-WDR34 could not rescue abnormal
262 IFT88 localization in WDR60 KO cells (Fig. S4D and S4Di).

263 *Defects in dynein-2 holocomplex assembly in absence of WDR34 or WDR60*

264 The results described above suggest a defect in the assembly of the dynein-2 holoenzyme and
265 therefore we used a proteomic approach to define the assembly of dynein-2. We stably expressed
266 HA-WDR34 in WT and WDR60 KO cells and HA-WDR60 in WT and WDR34 KO cells and performed
267 immunoprecipitations using HA-GFP as a control. Confirming that both WDR34 and WDR60 exist in
268 the same complex, immunoprecipitation analysis showed that in WT cells HA-WDR60 pulls down
269 WDR34, while HA-WDR34 pulls down WDR60 (Fig. S5A and S5B). Multiplex tandem-mass-tag (TMT)
270 labeling enabled us to define the interactome of WDR34 in the presence and absence of WDR60 and
271 of WDR60 in the presence and absence of WDR34. We found that the interactions of HA-WDR34
272 with dynein-2 components is reduced in WDR60 KO cells compared to WT cells (Fig. 10A). In
273 particular, loss of WDR60 caused a reduction of DHC2, DYNLRB1, TCTEX1D2, DYNLT1, DYNC2LI1 and
274 DYNLL2 immunoprecipitated with HA-WDR34 (Fig. 10B and 10Bi) compared to WT cells. Moreover,
275 interactions of HA-WDR34 with several IFT components and the molecular chaperone NudCD3 were
276 reduced in WDR60 KO cells. Surprisingly, HA-WDR60 interactions with dynein-2 components were
277 largely unchanged between WT and WDR34 KO cells (Fig. 10B and 10Bii); dynein-2 components

278 bound with similar efficiency to HA-WDR60 expressed either in WT and WDR34 KO cells, with a slight
279 but reproducible reduction in DHC2 and DYNLRB1 binding in WDR34 KO compared to WT cells.
280

281 ## Discussion

282 *Structural and functional asymmetry of the dynein-2 motor*

283 Our data provide evidence that the structural asymmetry with the dynein-2 motor is matched by
284 functional asymmetry. Perhaps most strikingly, we find that WDR34 is essential for axoneme
285 extension during early steps of ciliogenesis, whereas WDR60 is not required for ciliogenesis. Both
286 subunits are necessary for maintaining proper cilia protein composition. Depletion of WDR34 using
287 RNAi is also associated with ciliary defects (Asante et al., 2013) and patient fibroblasts have shorter
288 cilia with a bulbous tip (Huber et al., 2013). Fibroblasts from WDR34 knockout mice also have
289 stumpy cilia and defects in Shh signaling (Wu et al., 2017). It is intriguing that some cells missing
290 WDR34 can still extend a rudimentary cilium but even here, ciliary protein localization is severely
291 disrupted. Since WDR60 cells can extend an axoneme, WDR34 and WDR60 clearly have distinct but
292 overlapping functions in cells. We consider that WDR34 plays an essential role in ciliogenesis to
293 ensure delivery of a key factor required for axoneme extension. It is noteworthy that in the absence
294 of WDR34, WDR60 can still assemble effectively with the other subunits of dynein-2. While these
295 interactions are likely reduced compared to the normal situation, this shows that it is specifically
296 WDR34 that is required at this early stage of ciliogenesis. Our EM data show that it acts at a stage
297 after docking of the ciliary vesicle, immediately before axoneme extension. Paradoxically, our data
298 also show that in the absence of WDR60, the dynein-2 holocomplex cannot form effectively yet
299 axoneme extension occurs normally. This raises the possibility that WDR34 is itself required for
300 axoneme extension, possibly outside of the context of the dynein-2 complex. We cannot rule out
301 that there are dynein-2-independent functions of WDR34 and WDR60 but all data provide strong
302 evidence that they co-exist in the dynein-2 holoenzyme.

303 *Assembly of the dynein-2 holocomplex*

304 In WDR34 and WDR60 KO cells, LIC3 is no longer detected in primary cilia, while TCTEX1 localization,
305 a dynein light chain that is also a component of dynein-1, was unperturbed. Coupled with our
306 proteomics data, this suggests that the localization of LIC3 to cilia is a good reporter of dynein-2
307 assembly. Surprisingly we found that DHC2 levels at the ciliary base are reduced in WDR34 KO cells
308 compared to WT and WDR60 KO cells. Our data show that in WDR34 KO cells, the remaining
309 subunits can coassemble into partial dynein-2 complexes. We do not, however, know if this is a
310 functional or indeed processive motor. According to the current model based on work in *C. elegans*
311 and *Chlamydomonas*, the dynein-2 complex is transported by the kinesin-2 motor in the anterograde
312 direction, as a passive cargo, and at the tip it switches direction and it is converted in an active
313 motor (Chien et al., 2017; Mijalkovic et al., 2017; Pedersen et al., 2006; Toropova et al., 2017;

314 Williamson et al., 2012). Within this model, it is not known how dynein-2 is maintained in an inactive
315 state during anterograde trafficking. One possibility is that WDR34 might function in the final step of
316 dynein-2 complex assembly prior to motor activation, potentially at the ciliary tip. Support for this
317 comes from *C. elegans* where individual dynein-2 proteins show distinct turnaround times within
318 cilia (Li et al., 2015). It is of course not clear how much of the protein is incorporated within a dynein
319 complex in these experiments. The tight association of WDR34 with WDR60 and their functional
320 interdependence (loss of one leading to destabilization of the other) would argue against the
321 likelihood of dynamic subunit interchange during IFT. Further structural analysis could help resolve
322 this question. Interaction of WDR60 with WDR34 in our pull-down experiments indicates that each
323 dynein-2 complex contains both WDR34 and WDR60, in agreement with our own previously
324 reported data (Asante et al., 2014). Moreover, we found that stably expressed WDR60 could not
325 rescue ciliogenesis defects in WDR34 KO cells, neither could WDR34 rescue IFT88 localization defects
326 observed in WDR60 KO cells. Therefore WDR34 and WDR60 are not functionally redundant, at least
327 in this regard. This supports a model where WDR34 and WDR60 play different roles in ciliogenesis
328 and in IFT within the context of the dynein-2 complex, likely through different interactions with
329 distinct components.

330 *Ciliary trafficking defects in absence of WDR34 and WDR60*

331 Loss of either WDR34 or WDR60 leads to IFT particle accumulation at the base of as well as within
332 cilia. We found that loss of WDR60 results in an increase of IFT-B proteins, IFT20, IFT57, and IFT88,
333 not only at the tip but also close to the cilia base. This suggests that IFT-B proteins could be retained
334 at the basal body or around the transition zone. Consistent with these results, mutations in IFT-A or
335 dynein-2 in mice also result in abnormal accumulation of IFT particles near the base of the cilium
336 (Goggolidou et al., 2014; Liem et al., 2012; Ocbina et al., 2011). This has been linked to defects in the
337 export of ciliary cargo across the transition zone (He et al., 2017). Similar defects are seen following
338 disruption of the heavy chain, DHC2 (Hou and Witman, 2015).

339 In addition to defects in retrograde IFT, incomplete assembly of dynein-2 in WDR60 KO cells could
340 cause a block in IFT train assembly and impaired entry of cargo into cilia. Indeed, work in C. *elegans*
341 has shown that IFT-B is required for entry of dynein-2 into cilia (Yi et al., 2017). In addition to these
342 defects, we show that KAP3, a subunit of kinesin-2, accumulates at the ciliary tip of WDR60 KO cells.
343 This would decrease the levels of kinesin-2 available to load onto departing anterograde trains and
344 further cause accumulation of IFT particles at the base. This might also reflect some functional
345 coupling of dynein-2 and kinesin-2 in the assembly of anterograde IFT particles. This phenotype
346 might be exacerbated because those IFT-B particles that do enter become stuck at the ciliary tips in

347 WDR60 KO cells because of defects in retrograde IFT. Notably, our data are also consistent with
348 models where, in metazoa, kinesin-2 motors are returned to the ciliary base by dynein-2-dependent
349 retrograde IFT (Broekhuis et al., 2013; Chien et al., 2017; Mijalkovic et al., 2017; Prevo et al., 2015;
350 Signor et al., 1999; Williams et al., 2014) but contrasts with *Chlamydomonas* where kinesin-2
351 diffuses back to the cilia base (Engel et al., 2012). Overall, our data support models where dynein-2
352 acts both in loading of cargo into cilia and in exit from cilia.

353 These findings suggest a complex interplay between IFT particles and IFT motors to control entry to
354 and exit from cilia. Notably, interfering with either dynein-2 or IFT results in perturbation of
355 transition zone organization, IFT, and ciliary membrane protein localization (Garcia-Gonzalo and
356 Reiter, 2017).

357 *Dynein-2 is required for transition zone composition*

358 The transition zone is the ciliary region most proximal to the mother centriole and it functions as a
359 gate, acting as a diffusion barrier to prevent unregulated entry of high molecular weight proteins
360 and maintaining the protein composition of the ciliary membrane (Garcia-Gonzalo and Reiter, 2017;
361 Jensen and Leroux, 2017). Our results show that loss of either dynein-2 intermediate chain disrupts
362 the organization of the ciliary transition zone. The defect is clearly very significant since we observe
363 accumulation of intraciliary vesicles within the cilia of WDR60 KO cells that would normally be
364 excluded by the diffusion barrier. To our knowledge, such structures have not been described
365 previously and would suggest a significant defect in the diffusion barrier and/or gated entry
366 mechanisms. The role of dynein-2 in maintaining transition zone composition is also consistent with
367 the fact that LIC3 and overexpressed WDR34 and WDR60 localize at the transition zone in RPE1 cells.
368 Moreover, in a previous study, active phosphorylated TCTEX1 has been detected at the transition
369 zone of neural progenitors (Li et al., 2011). Changes in transition zone composition are associated
370 with a reduced localization of soluble and membrane proteins in the cilia (Berbari et al., 2008b; Chih
371 et al., 2011). 5HT6, SSTR3, and Arl13B are all reduced in abundance within cilia of WDR60 KO cells,
372 suggesting that these proteins might not be effectibvvely retained within cilia, but leak out through
373 the diffusion barrier. The alternative, as discussed above, is that these proteins are less effectively
374 loaded into cilia. We did not find a difference in the intensity levels of overexpressed Rab8a in
375 WDR60 KO compared to WT cells suggesting that at least some proteins can enter normally. It seems
376 likely that the defects we see in both entry to, and exit from, cilia in these KO cells are caused by
377 defects in transition zone structure.

378 *Dynein-2 dysfunction and disease*

379 The list of mutations causing disease in genes associated with primary cilia is continuously
380 expanding. Our results show that Smo localization is deregulated in the absence of WDR60. Smo is
381 thought to enter cilia continuously but rapidly exit in the absence of ligand. Our data are consistent
382 with this, with loss of WDR60 results in aberrant accumulation of Smo in cilia and likely to perturbed
383 hedgehog signaling. Interestingly, abnormal accumulation of Smo in the cilia has also been observed
384 in mouse fibroblasts with mutations in DHC2. In these mutant mice inactivation of dynein-2 causes
385 loss of Shh signaling and midgestation lethality (Ocbina et al., 2011). Given the links between
386 hedgehog signaling and skeletogenesis, this is likely to be a major cause of the phenotypes seen on
387 loss-of-function of dynein-2 in animal models and in patients (Dagoneau et al., 2009; Li et al., 2015;
388 May et al., 2005; Wu et al., 2017).

389 In this study, we also characterized the function of dynein-2 using disease-causing mutations found
390 in SRPs and JATD syndromes. Using mutagenesis to recreate patient mutations WDR60[Q631*] and
391 WDR60[T749M], we show that the N-terminal region of WDR60 is sufficient to bind to WDR34 and
392 TCTEX1 but not to LIC3. This suggests some assembly of a WDR34-WDR60 module prior to full
393 complex assembly. Further analysis of patient mutation [Q631*] reveals that the C-terminal β-
394 propeller domain of WDR60 is required for binding of the IFT-B proteins, including IFT88. The
395 observed reduction in binding between the WDR60[Q631*] mutant and NudCD3 is expected as the
396 NudC family acts as co-chaperones with hsp90 for folding of β-propellers such as WD repeat
397 domains (Taipale et al., 2014). In contrast, WDR60[T749M] binds to other dynein-2 proteins, IFT
398 proteins, and NudCD3. The reduction in binding to LIC3 seen with this mutation suggests that less
399 efficient dynein-2 assembly might contribute to the patient phenotypes.

400 Surprisingly, expression of WT and WDR34[A22V] or [C148F] mutants in WDR34 KO cells was able to
401 rescue both normal cilia length and normal IFT88 localization at the cilia base. Genome sequencing
402 data showed that patients with WDR34[A22V] mutation also present mutations in DYNC2H1 and
403 IFT140 (Schmidts et al., 2013b), similarly, a second mutation in the WDR34 gene was found in
404 patients with [C148F] mutant. Thus, it is possible that these two mutant proteins are not sufficient to
405 impair dynein-2 function themselves and exclusively cause a deleterious effect when a second
406 modification is also present.

407 Our data show that not only is dynein-2 required for retrograde IFT but also to build and maintain a
408 functional diffusion barrier at the base of the cilium. Our data do not discriminate between roles in
409 assembly versus maintenance of the transition zone. Other recent work has shown that Joubert

syndrome is caused by disruption of the transition zone (Shi et al., 2017). Joubert syndrome leads to severe neurological effects that are underpinned by developmental defects in hedgehog signaling. Jeune syndrome is characterized by skeletal defects but these are attributed to hedgehog signaling defects. Together our work and that of Shi et al. (2017) suggests that defects in transition zone architecture and resulting defects in developmental signaling might define a common root cause of both Joubert and Jeune syndromes, and indeed perhaps other ciliopathies.

Acknowledgements

We would like to thank Katharine Risk, Beth Moyse, and Imogen Binnian for their contributions to the work and Janine McCaughey for helpful discussion on this work. This work was supported by grants from the BBSRC (BB/N000420/1) and MRC (MR/P000177/1 and MR/K018019/1). We would like to thank the Wolfson Bioimaging Facility for support of the microscopy experiments. Confocal microscopy was supported by a BBSRC ALERT 13 capital grant (BB/L014181/1).

The authors declare no competing financial interests.

Author contributions: DJS, LV, and NLS conceived and designed the experiments and wrote the manuscript. LV and NJS performed the experiments and analyzed the data. KJH helped design and conducted the proteomics experiments and data analysis.

428 ## Materials and Methods

429 All reagents were purchased from Sigma-Aldrich (Poole, UK) unless stated otherwise.

430 *Plasmids, cloning, and mutagenesis.*

431 The human WDR34 gene was obtained from the Origene (SC319901, Cambridge Bioscience), human
432 WDR60 was generated by gene synthesis (Life Technologies, Paisley, UK). An HA tag for WDR34 and
433 WDR60 was added by PCR and both proteins were subcloned in the pLVX-puro vector. Mutant
434 [T749M WDR60] was generated by site-directed mutagenesis PCR using the primers: Fw: 5'-
435 CAGAACCGCCatgTTCTCCACC-3' and Rv 5'-GGTGGAGAACATGGCGGTTCTG-3' changing codon ACG
436 (Threonine) to ATG (Methionine). WDR60 [Q631*] mutant was constructed by site-directed
437 mutagenesis using the primers: Fw: 5'-GATAGCAGCTCCtagCTGAATACC-3' and 5'-
438 GGTATTCAGCTAGGAGCTGCTATC-3' changing codon CAG (Glutamine) to TAG (STOP codon). For
439 WDR34, the A22V mutant was generated by changing codon GCG (Alanine) to GTC (Valine) using
440 oligonucleotides 5'-TGCGGCGCTGgtgACAGTCGGGG-3' and 5'-ACACCAGCGCTTCCCGCCTG-3'. The
441 C148F mutation was generated by changing codon TGT (Cysteine) to TTT (Phenylalanine) using
442 oligonucleotides 5'-GATGGTGTCTtttCTGTATACCCTGGG-3' and 5'-TGCTGCTGCTCGGTCCAG-3'. All
443 constructs were validated by DNA sequencing.

444 Mouse L13-Arl13b-GFP was a gift from Tamara Caspary (Addgene plasmid # 40879, (Larkins et al.,
445 2011)), IFT20-GFP ((Follit et al., 2006), plasmid JAF2.13) was a gift from Gregory Pazour (Addgene
446 plasmid # 45608). pEGFPN3-SSTR3 and pEGFPN3-5HT6 were gifts from Kirk Mykytyn (Addgene
447 plasmid #35624 and #35623, (Berbari et al., 2008a)), EGFP-Rab8 was a gift from Johan Peränen
448 (University of Helsinki).

449 *Cell culture*

450 Human telomerase-immortalized retinal pigment epithelial cells (hTERT-RPE-1, ATCC CRL-4000) were
451 grown in DMEM-F12 supplemented with 10% FBS (Life Technologies, Paisley, UK) at 37°C under 5%
452 CO_2. Cells were not validated further after purchase from ATCC. Transient transfections of Arl13b-
453 GFP, SSTR3-GFP, 5HT6-GFP, and Rab8-GFP were performed using Lipofectamine 2000 (Life
454 Technologies, Paisley, UK) according to the manufacturer's protocol. Lentiviral particles for each of
455 the stable RPE-1 cell lines were produced in HEK293T cells using the Lenti-XTM HTX Packaging
456 System (Clontech, Saint-Germain-en-Laye, France). Low passage hTERT-RPE1 cells were transduced
457 with the resultant viral supernatant, strictly according to the manufacturer's directives and at 48 h
458 post-transduction, cells were subcultured in presence of 5 µg/ml puromycin. RPE-1 cells were
459 incubated in serum-free medium for 24 h to induce ciliogenesis. Confluent cells were placed in

460 serum-free media and treated with Shh agonist SAG (Selleckchem (from Stratech Scientific, Ely, UK)
461 Catalog No.S7779) at the final concentration of 100 nM for 24 h.

462 *Genome engineering*

463 The guide RNAs (gRNA) targeting WDR34 were designed using 'chop chop' software (Labun et al.,
464 2016) or using CRISPR design http://crispr.mit.edu/ for designing WDR60 gRNA (Hsu et al., 2014).
465 pSpCas9(BB)-2A-GFP (Addgene plasmid, #PX458) was used as the vector to generate a gRNA. The
466 gRNA sequences (5'- A GCC TTT CTT CGG AGA GTG G-3'; and 5'-CA GGT GTC TTG TCT GTA TAC -3')
467 were designed to target Exon2 and Exon3 of human WDR34. Similarly, the gRNA (5'-AG GTG CAG
468 GGA TCC CGA CCA-3') was designed to target exon 3 of WDR60. RPE-1 cells were transfected with 1
469 µg of pSpCas9(BB)-2A-GFP. After 48 h GFP-positive cells were sorted, and singles cells were plated in
470 a 96 well plate. To check the WDR34 and WDR60 genes, genomic DNAs of the target sequences were
471 extracted and subjected to PCR. Subsequently, the PCR products were cloned in the pGEM® T Easy
472 vector according to the manufacturer's instructions and sequenced. In three cells clones, identified
473 as WDR34 KO#1, WDR34 KO#2 and WDR60 KO, small deletions/insertions causing a frameshift were
474 detected in both alleles (Supplementary Fig. 1 for details). On the contrary, the cell clones identified
475 as CRISPR CTRL WDR34 and WDR60 cells, transfected and treated in the same conditions of our
476 knock out clones, did not show any mutation in the targeted genomic DNA region.

477 *Antibodies*

478 The antibodies used, and their dilutions for western blotting (WB) and immunofluorescence (IF) are
479 as follows: Acetylated tubulin (Sigma (Poole, UK) T6793 1:2000 for IF), rabbit anti-HA (Cell Signaling
480 Technologies (New England Biolabs, Hitchin, UK) 1:2000 WB, 1:1000 IF), rabbit IFT88 (Proteintech
481 (Manchester, UK) 13967-1-AP, 1:200 WB, 1:300 IF), rabbit anti-IFT140 (Proteintech 17460-1-AP,
482 1:200, WB 1:100 IF), rabbit anti-IFT57 (Proteintech 11083-1,-AP 1:200, WB 1:100 IF), rabbit anti-
483 IFT43 (Proteintech 24338-1-AP, 1:50 IF), anti-IFT20 (Proteintech 13615-1-AP, 1:200 IF), anti-TMEM67
484 (proteintech13975-1-AP, 1:50 IF), anti-RPGRIP1L (Proteintech 55160-1-AP, 1:100 IF), anti-DYNC2HC1
485 (Proteintech 55473-1-AP, 1:100 IF), rabbit anti-LIC3 (Proteintech 15949-1-AP, 1:250 WB, 1:100 IF),
486 rabbit anti-TCTEX1 (Santa Cruz Biotechnology (from Insight Biotechnology, Wembley, UK) sc-28537,
487 1:200 WB, 1:100 IF), rabbit anti-Arl13B (Proteintech 17711-1AP, 1:1000 IF), rabbit anti-TCTN1
488 (Proteintech 15004-1-AP, 1:100 IF), rabbit anti-Smo (Abcam (Cambridge, UK) ab38686, 1:100 IF),
489 Sheep anti-Myc ((Fan et al., 2010) kindly provided by Harry Mellor, University of Bristol), rabbit anti-
490 WDR60 (Novus Biologicals (from Bio-Techne Abingdon, UK) NBP1-90437 1:300 WB in Fig.9), rabbit
491 anti-WDR60 (Sigma HPA021316, 1:300 WB in Fig. S2 and Fig.S5), rabbit anti-WDR34 (Novus
492 NBP188805, 1:300 WB), mouse anti-GAPDH (Abcam ab9484, 1:1000 WB), p150 glued (BD 6127009,

493 1:1000 WB), LIS1 (Bethyl A300-409A, 1:1000 WB), dic74 (MAB1618 Millipore (Watford, UK), 1:1000
494 WB), NUDCD3 (Sigma HPA019136, 1:350 WB).

495 *Immunofluorescence*

496 Cells grown on 0.17 mm thick (#1.5) coverslips (Fisher Scientific, Loughborough, UK) were washed in
497 PBS, and then fixed for 10 min in PFA and permeabilized with PBS containing 0.1% Triton X-100 for 5
498 min. Alternatively, cells were fixed in ice-cold methanol at −20°C for 5 min for TMEM67, RPGRIP1L,
499 TCTN1, DYNC2H1 and IFT20 staining.

500 For TCTEX1 immunolabelling, cells were washed twice with pre-warmed cytoskeletal buffer (CB,
501 containing 100 mM NaCl 300 mM sucrose, 3 mM MgCl2, and 10 mM PIPES) and fixed for 10 min in
502 CB-PFA, as described previously (Hua and Ferland, 2017).Subsequently, cells were blocked using 3%
503 BSA in PBS for 30 min at room temperature. The coverslips were incubated with primary antibodies
504 for 1 h at room temperature, washed in PBS and then incubated with secondary antibodies for
505 another 1 h at room temperature. Nuclear staining was performed using DAPI [4,6-diamidino-2-
506 phenylindole (Life Technologies), diluted at 1:5000 in PBS] for 3 min at room temperature, and the
507 cells were then rinsed twice in PBS. Cells were imaged using an Olympus IX- 71 or IX-81 widefield
508 microscope with a 63x objective, and excitation and emission filter sets (Semrock, Rochester, NY)
509 controlled by Volocity software (version 4.3, Perkin-Elmer, Seer Green, UK). Alternatively, cells in Fig.
510 4 and Fig. 7 were imaged using Leica SP5 confocal microscope (Leica Microsystems, Milton Keynes,
511 UK). Live images in Fig. 3 were imaged using Leica SP8. All images were acquired as 0.5 µm z-stacks.
512 All graphs show mean and standard deviation.

513 *Rescue experiments*

514 For 'rescue' experiments, stable WDR60 KO cell lines overexpressing wild-type and mutants HA-
515 tagged WDR60 were generated. Similarly, WDR34 KO#1 cells were stably transfected with WT and
516 mutants WDR34 tagged with a GFP. Cells were serum starved for 24 h, fixed and processed for
517 immunofluorescence analysis.

518 *Electron microscopy*

519 Cells were serum starved 24 h and fixed in 2.5% glutaraldehyde for 20 min. Next, the cells were
520 washed for 5 min in 0.1 M cacodylate buffer then post-fixed in 1% OsO_4/0.1 M cacodylate buffer for
521 30 min. Cells were washed 3x with water and stained with 3% uranyl acetate for 20 min. After
522 another rinse with water, cells were dehydrated by sequential 10 min incubations with 70, 80, 90,
523 96, 100 and 100% ethanol before embedding in Epon™ at 70°C for 48 h. Thin (70 nm) serial sections
524 were cut and stained with 3% uranyl acetate then lead citrate, washing 3x with water after each.

525 Once dried, sections were imaged using an FEI (Cambridge, UK) Tecnai12 transmission electron
526 microscope.

527 *Immunoblotting*

528 Cells were lysed in buffer containing 50 mM Tris pH7.5, 150 mM NaCl, 1% Igepal and 1 mM EDTA.
529 Samples were separated by SDS-PAGE followed by transfer to nitrocellulose membranes.
530 Membranes were blocked in 5% milk-TBST. Primary antibodies diluted in blocking buffer were
531 incubated with membrane overnight and detected using HRP-conjugated secondary antibodies
532 (Jackson ImmunoResearch, West Grove, PA) and enhanced chemiluminescence (GE Healthcare,
533 Cardiff, United Kingdom).

534 *Fluorescence intensity measurement*

535 Quantification of fluorescence intensity was performed using original images. Measurement of
536 intensity was performed using the average projections of acquired z-stacks of the area of the ciliary
537 marker acetylated tubulin. Fluorescence intensity along the ciliary axoneme was measured using
538 ImageJ plot profile tool. Fluorescence intensity in at the ciliary base was measured drawing same
539 diameter circles at the ciliary base.

540 *Immunoprecipitation*

541 RPE-1 cells expressing the indicated cDNA constructs were washed with PBS and incubated with the
542 crosslinker solution (1 mM DSP, Thermo Fisher Scientific #22585) for 30 min on ice. The reaction was
543 quenched by adding 500 mM Tris-HCl pH 7.5 for 15 min. Cells were washed twice with PBS and lysed
544 in a buffer containing 50 mM Tris/HCl, pH 7.4, 1 mM EDTA, 150 mM NaCl, 1% Igepal and protease
545 inhibitors (539137, Millipore). Subsequently, cells were incubated on a rotor at 4˚C for 30 min and
546 then lysates were centrifuged at 13,000 g at 4˚C for 10 min. Cell lysates were added to the
547 equilibrated anti-HA-Agarose beads (Sigma A2095, batch number 026M4810V) and incubated on a
548 rotor at 4˚C. Next, the beads were washed three times by centrifuging at 2000 g for 2 min at 4˚C with
549 1 ml of washing buffer (50 mM Tris-HCl, 150 mM NaCl, 0.5 mM EDTA, Triton X-100 0.3% SDS 0.1%)
550 containing protease inhibitors (539137, Millipore). Samples used for SDS-PAGE and immunoblotting
551 were resuspended in 50 µl of LDS sample buffer (Life Technologies) containing sample reducing
552 agent (Life Technologies) and boiled at 95˚C for 10 min.

553 *Proteomic analysis*

554 For TMT Labelling and high pH reversed-phase chromatography, the samples were digested from the
555 beads with trypsin (2.5 µg trypsin, 37°C overnight), labeled with Tandem Mass Tag (TMT) six-plex
556 reagents according to the manufacturer's protocol (Thermo Fisher Scientific, Loughborough, UK) and

557 the labeled samples pooled. The pooled sample was then desalted using a SepPak cartridge
558 according to the manufacturer's instructions (Waters, Milford, Massachusetts, USA)). Eluate from
559 the SepPak cartridge was evaporated to dryness and resuspended in buffer A (20 mM ammonium
560 hydroxide, pH 10) prior to fractionation by high pH reversed-phase chromatography using an
561 Ultimate 3000 liquid chromatography system (Thermo Fisher Scientific). In brief, the sample was
562 loaded onto an XBridge BEH C18 Column (130 Å, 3.5 µm, 2.1 mm X 150 mm, Waters, UK) in buffer A
563 and peptides eluted with an increasing gradient of buffer B (20 mM ammonium hydroxide in
564 acetonitrile, pH 10) from 0-95% over 60 min. The resulting fractions were evaporated to dryness and
565 resuspended in 1% formic acid prior to analysis by nano-LC MSMS using an Orbitrap Fusion Tribrid
566 mass spectrometer (Thermo Fisher Scientific).

567 *Nano-LC Mass Spectrometry*

568 High pH RP fractions were further fractionated using an Ultimate 3000 nano-LC system in line with
569 an Orbitrap Fusion Tribrid mass spectrometer (Thermo Fisher Scientific). In brief, peptides in 1%
570 (vol/vol) formic acid were injected onto an Acclaim PepMap C18 nano-trap column (Thermo Fisher
571 Scientific). After washing with 0.5% (vol/vol) acetonitrile 0.1% (vol/vol) formic acid, peptides were
572 resolved on a 250 mm × 75 µm Acclaim PepMap C18 reverse phase analytical column (Thermo Fisher
573 Scientific) over a 150 min organic gradient, using 7 gradient segments (1-6% solvent B over 1 min., 6-
574 15% B over 58 min., 15-32% B over 58 min., 32-40% B over 5 min., 40-90% B over 1 min., held at 90%
575 B for 6 min and then reduced to 1% B over 1 min.) with a flow rate of 300 nl min−1. Solvent A was
576 0.1% formic acid and Solvent B was aqueous 80% acetonitrile in 0.1% formic acid. Peptides were
577 ionized by nano-electrospray ionization at 2.0 kV using a stainless steel emitter with an internal
578 diameter of 30 µm (Thermo Fisher Scientific) and a capillary temperature of 275°C.

579 All spectra were acquired using an Orbitrap Fusion Tribrid mass spectrometer controlled by Xcalibur
580 2.0 software (Thermo Fisher Scientific) and operated in data-dependent acquisition mode using an
581 SPS-MS3 workflow. FTMS1 spectra were collected at a resolution of 120 000, with an automatic gain
582 control (AGC) target of 400 000 and a max injection time of 100 ms. Precursors were filtered with an
583 intensity range from 5000 to 1E20, according to charge state (to include charge states 2-6) and with
584 monoisotopic precursor selection. Previously interrogated precursors were excluded using a
585 dynamic window (60 s +/- 10 ppm). The MS2 precursors were isolated with a quadrupole mass filter
586 set to a width of 1.2 m/z. ITMS2 spectra were collected with an AGC target of 10 000, max injection
587 time of 70 ms and CID collision energy of 35%.

588 For FTMS3 analysis, the Orbitrap was operated at 30 000 resolution with an AGC target of 50 000
589 and a max injection time of 105 ms. Precursors were fragmented by high energy collision

590 dissociation (HCD) at a normalized collision energy of 55% to ensure maximal TMT reporter ion yield.
591 Synchronous Precursor Selection (SPS) was enabled to include up to 5 MS2 fragment ions in the
592 FTMS3 scan.

593 *Data Analysis*

594 The raw data files were processed and quantified using Proteome Discoverer software v2.1 (Thermo
595 Fisher Scientific) and searched against the UniProt Human database (140000 entries) and GFP
596 sequence using the SEQUEST algorithm. Peptide precursor mass tolerance was set at 10 ppm, and
597 MS/MS tolerance was set at 0.6 Da. Search criteria included oxidation of methionine (+15.9949) as a
598 variable modification and carbamidomethylation of cysteine (+57.0214) and the addition of the TMT
599 mass tag (+229.163) to peptide N-termini and lysine as fixed modifications. Searches were
600 performed with full tryptic digestion and a maximum of 1 missed cleavage was allowed. The reverse
601 database search option was enabled and the data was filtered to satisfy false discovery rate (FDR) of
602 5%.
603

604 ## Figure Legends

605 *Figure 1: Role of dynein-2 intermediate chains WDR34 and WDR60 in ciliogenesis.*

606 (A) Cilia stained with the markers Arl13b (green) and acetylated tubulin (AcTub, red) in RPE1 WDR60
607 and WDR34 KO cell lines. Scale bars 5µm. (B) Percentage of ciliated cells (n=3; 656 WT, 430 WDR34
608 KO#1, 296 WDR34 KO#2, 397 WDR34 KO CTRL, 343 WDR60 KO and 195 WDR60 KO CTRL cells
609 quantified). (C) Cilia length in WDR60 and WDR34 KO compared with WT cells and CRISPR control
610 cells lines (n=3; 120 WT, 158 WDR60 KO, 138 WDR60 KO CTRL and 30 WDR34#1 cells quantified).
611 Mann-Whitney test was used, p-value: ****=<0.0001. (D- Hi) Representative 70 nm thick EM
612 sections of (D) WT, (E) WDR34 KO and (F, G- Hi) WDR60 KO cilia. (E) Six serial sections through a
613 WDR34 KO cilium showing no axoneme extension. (G) Two serial sections through a WDR60 KO
614 cilium showing. Arrows point to the bulbous ciliary tip and to a membrane protrusion containing
615 membrane vesicles; enlargements are shown to the right (H and Hi). Scale bar length and
616 magnification is indicated on the images.

617

618 *Figure 2: WDR34 and WDR60 are essential for IFT-B trafficking in primary cilia.*
619 (A, B) Localization of (A) IFT88 and (B) IFT57 in WT, WDR60 KO, and WDR34 KO#1 cells. Line graphs
620 show lines scans of IFT intensity along the length of a representative cilium from WT (Ai and Bi,
621 green), WDR60 KO (Aii and Bii, orange) and WDR34 KO (Aiii and Biii, yellow) cells. (C, D)
622 Quantification of IFT-B localization within cilia in WT and WDR60 KO cells (C, IFT88 102 WT and 101
623 WDR60 cells quantified; D, IFT57 106 WT and 98 WDR60 KO cells quantified; n=3 independent
624 experiments). Mann-Whitney test was used, p-value: ****=<0.0001. (E) Endogenous IFT20
625 accumulates at the ciliary tip in WDR60 KO cells. (F) Quantification of IFT20 localization within cilia in
626 WDR60 KO cells (n=3 independent experiments, 102 WT and 100 WDR60 KO cells quantified). (G)
627 Localization of IFT20-GFP in WT and WDR60 KO fixed cells. Scale bar, all panels = 5 µm.

628

629 *Figure 3: IFT-A trafficking defects in absence of WDR34 and WDR60.*

630 (A-B) Localization of IFT-A proteins (A) IFT140 and (B) IFT43 in WT, WDR60 KO, and WDR34 KO#1
631 cells. Line graphs show lines scans of IFT intensity along the length of a representative cilium from
632 WT (Ai and Bi, green), WDR60 KO (Aii and Bii, orange) and WDR34 KO (Aiii and Biii, yellow) cells. (C)
633 Quantification of IFT140 intensity within cilia in WT and WDR60 KO cells (n=3, 186 WT and 166
634 WDR60 KO cells quantified). (D) Quantification of the number of IFT43 positive cilia from WT and
635 WDR60 KO cells (n=3, 271 WT and 203 WDR60 KO cells quantified). (C-D) Mann-Whitney test was

636 used, p-value: ****=<0.0001. (E) Localization of KAP3A in WT, WDR60 KO, and WDR34 KO cells.
637 Scale bars = 5µm.

638

639 *Figure 4: WDR60 is crucial for the composition of cilia membrane proteins.*

640 (A and B) Single frame images are taken from live imaging movies of WT and WDR60 KO cells
641 overexpressing EGFP-SSTR3 and GFP-Arl13b. (C-F) Fixed cell staining of overexpressed Arl13b-GFP,
642 EGFP-SSTR3, EGFP-5HT6, and EGFP-Rab8a in WT and WDR60 KO cells. (Ci-Fi) Intensity quantification
643 of the overexpressed protein indicated (Arl13b-GFP n=3, 56 WT and 50 WDR60 KO cells quantified;
644 EGFP-SSTR3 n=3, 80 WT and 50 WDR60 KO cells quantified; EGFP-5HT6 n=3, 50 WT and 51 WDR60
645 KO cells quantified; EGFP-Rab8a n=3, 51 WT and WDR60 50 KO cells quantified). Mann-Whitney test
646 was used, p-value: ****=<0.0001. Scale bars 5µm.

647

648 *Figure 5: Dynein-2 is important for transition zone assembly.*

649 (A-C) Localization of RPGRIP1L, TMEM67, and TCTN1 in WT and KO cells. (Ai and Bi) Percentage of
650 RPGRIP1L and TMEM67 positive cilia. RPGRIP1L n=3, 188 WT and 272 WDR60 KO cells quantified;
651 TMEM67 n=3, 359 WT and 243 WDR60 KO cells quantified. Mann-Whitney test was used p-value:
652 ****=<0.0001. Scale bars 5µm.

653

654 *Figure 6: Loss of WDR60 affects Smo localization in the cilia*

655 (A and B) Immunofluorescence of WT and WDR60 KO cells in presence or absence of SAG and
656 stained for Smo (green), AcTub (red), and DAPI (blue). (Ai and Bi) Percentage of Smo positive cilia in
657 SAG untreated (n=3, 148 WT and 120 WDR60 KO cells quantified) and treated cells (n=3, 670 WT and
658 580 WDR60 KO cells quantified). (Bii) Qquantification of total intensity of ciliary Smo labelling in cells
659 treated with SAG (n=3, 102 WT and 82 WDR60 KO cells quantified). Mann-Whitney test was used, p-
660 value: ****=<0.0001. Scale bars 5µm.

661

662 *Figure 7: WDR34 and WDR60 KO rescue experiments.*

663 (A) Immunofluorescence staining of HA (green) in WDR60 KO cell lines stably expressing HA-tagged
664 WT and mutant WDR60 constructs. (B and C) IFT88 or IFT140 staining (green) with AcTub labeling
665 (red) of the stable cell lines shown in A as well as WT cells. (Bi) Total intensity quantification of IFT88

666 labeling across the length of primary cilia in each cell line (n=3; 97 WT, 125 WDR60 KO, 202 WDR60
667 KO+ HA-WDR60, 119 WDR60 KO+ HA-WDR60 [T749M], 150 WDR60 KO+ HA-WDR60 [Q631*] cells
668 quantified). (Ci) Total intensity quantification of IFT140 labeling across the length of primary cilia in
669 each cell line (n=3; 168 WT, 164 WDR60 KO, 63 WDR60 KO+ HA-WDR60, 56 WDR60 KO+ HA-WDR60
670 [T749M], 71 WDR60 KO+ HA-WDR60 [Q631*] cells quantified). (D and E) WDR34 KO#1 cells stably
671 expressing mGFP-tagged WT and mutant WDR34. (D) Primary cilia staining with Arl13b (red) and
672 AcTub (blue). (Di) Percentage of ciliated cells (n=3; 357 WT, 430 WDR34 KO, 399 WDR34 KO + mGFP-
673 WDR34, 383 WDR34 KO + mGFP-WDR34 [A22V], 432 WDR34 KO + mGFP-WDR34[C148F] cells
674 quantified). (E) IFT88 staining in WT, WDR34 KO#1 cells, and WDR34 KO#1 cells expressing GFP-
675 tagged WT and mutant WDR34. One-way ANOVA followed by Kruskal-Wallis test was used p-value:
676 ****=<0.0001.

677

678 *Figure 8: Disease-associated mutations affect dynein-2 interactions.*

679 (A-C) Immunoprecipitation of HA-tagged GFP, WT, WDR60 [T749M] and HA-WDR60 [Q631*] mutant
680 proteins followed by immunoblot for (A) HA, NudCD3, and GAPDH; (B) WDR34, LIC3, and TCTEX1and
681 (C) IFT140, IFT88, and IFT57.

682

683 *Figure 9: Dynein-2 assembly in primary cilium.*

684 (A) Immunoblotting for WDR60 and WDR34 in WT, WDR34 KO#1 and WDR60 KO cells. (B) LIC3
685 localization in the cilia of WT, WDR34 KO#1 and WDR60 KO cells. (C) DHC2 localization at the ciliary
686 base in WT and KO cells. (Ci) Intensity quantification shows a reduction of DHC2 at the ciliary base in
687 WDR34 KO#1 cells (n=3, 120 WT, 106 WDR60 KO and 71 WDR34 KO #1 cells quantified). (D) TCTEX1
688 localizes at the ciliary base in WT and KO cells (n=3 115 WT, 85 WDR60 KO, and 50 WDR34 KO#1
689 cells quantified). Mann-Whitney test ,p-value: ****=<0.0001. Scale bars 5µm.

690

691 *Figure 10: Proteomics of HA-WDR34 and HA-WDR60 interactomes in knockout cell lines.*

692 Abundance ratios in WT/ WDR34 KO cells expressing HA-WDR60 and WT/ WDR60 KO cells
693 expressing HA-WDR34 determined by TMT analysis. Proteomic data were obtained from two
694 independent experiments. The table shows raw data from one experiment. Similar results were
695 obtained by normalizing the data with respect to the overexpressed protein abundance. (B)
696 Schematic of the dynein-2 complex; the heavy chain is shown as two light blue homodimers, light

697 intermediate chains are shown as hexagons, intermediate chains as extended ovals and light chains
698 as circles. (Bi and Bii) Model of the dynein-2 complex in absence of (Bi) WDR60 or (Bii) WDR34.
699 Reduced binding is represented by decreased color intensity. (Bi) In WDR60 KO cells interaction of
700 HA-WDR34 with DHC2, DYNC2LI1/LIC3, DYNLT1/TCTEX1, DYNLL1/LC8-1, DYNLL2/LC8-2, TCTEX1D2,
701 and DYNLRB1 is greatly reduced respect to WT cells. (Bii) In WDR34 KO cells interaction of HA-
702 WDR60 with other components of dynein-2 is mostly unchanged.
703

704 ## References

705 Asante, D., L. Maccarthy-Morrogh, A.K. Townley, M.A. Weiss, K. Katayama, K.J. Palmer, H. Suzuki, C.J.
706 Westlake, and D.J. Stephens. 2013. A role for the Golgi matrix protein giantin in ciliogenesis
707 through control of the localization of dynein-2. *J. Cell Sci.* 126:5189-5197.

708 Asante, D., N.L. Stevenson, and D.J. Stephens. 2014. Subunit composition of the human cytoplasmic
709 dynein-2 complex. *J. Cell Sci.* 127:4774-4787.

710 Berbari, N.F., A.D. Johnson, J.S. Lewis, C.C. Askwith, and K. Mykytyn. 2008a. Identification of ciliary
711 localization sequences within the third intracellular loop of G protein-coupled receptors. *Mol*
712 *Biol Cell*. 19:1540-1547.

713 Berbari, N.F., J.S. Lewis, G.A. Bishop, C.C. Askwith, and K. Mykytyn. 2008b. Bardet-Biedl syndrome
714 proteins are required for the localization of G protein-coupled receptors to primary cilia.
715 *Proc Natl Acad Sci U S A*. 105:4242-4246.

716 Broekhuis, J.R., S. Rademakers, J. Burghoorn, and G. Jansen. 2013. SQL-1, homologue of the Golgi
717 protein GMAP210, modulates intraflagellar transport in C. elegans. *J. Cell Sci.* 126:1785-
718 1795.

719 Chen, L.S., S.J. Shi, P.S. Zou, M. Ma, X.H. Chen, and D.H. Cao. 2016. Identification of novel DYNC2H1
720 mutations associated with short rib-polydactyly syndrome type III using next-generation
721 panel sequencing. *Genetics and Molecular Research*. 15.

722 Chien, A., S.M. Shih, R. Bower, D. Tritschler, M.E. Porter, and A. Yildiz. 2017. Dynamics of the IFT
723 machinery at the ciliary tip. *Elife*. 6:1-25.

724 Chih, B., P. Liu, Y. Chinn, C. Chalouni, L.G. Komuves, P.E. Hass, W. Sandoval, and A.S. Peterson. 2011.
725 A ciliopathy complex at the transition zone protects the cilia as a privileged membrane
726 domain. *Nat. Cell Biol.* 14:61-72.

727 Cossu, C., F. Incani, M.L. Serra, A. Coiana, G. Crisponi, L. Boccone, and M.C. Rosatelli. 2016. New
728 mutations in DYNC2H1 and WDR60 genes revealed by whole-exome sequencing in two
729 unrelated Sardinian families with Jeune asphyxiating thoracic dystrophy. *Clin. Chim. Acta*.
730 455:172-180.

731 Criswell, P.S., L.E. Ostrowski, and D.J. Asai. 1996. A novel cytoplasmic dynein heavy chain: expression
732 of DHC1b in mammalian ciliated epithelial cells. *J. Cell Sci.* 109 (Pt 7):1891-1898.

733 Dagoneau, N., M. Goulet, D. Genevieve, Y. Sznajer, J. Martinovic, S. Smithson, C. Huber, G. Baujat, E.
734 Flori, L. Tecco, D. Cavalcanti, A.L. Delezoide, V. Serre, M. Le Merrer, A. Munnich, and V.
735 Cormier-Daire. 2009. DYNC2H1 mutations cause asphyxiating thoracic dystrophy and short
736 rib-polydactyly syndrome, type III. *Am. J. Hum. Genet.* 84:706-711.

737 El Hokayem, J., C. Huber, A. Couvé, J. Aziza, G. Baujat, R. Bouvier, D.P. Cavalcanti, F.A. Collins, M.-P.
738 Cordier, A.-L. Delezoide, M. Gonzales, D. Johnson, M. Le Merrer, A. Levy-Mozziconacci, P.
739 Loget, D. Martin-Coignard, J. Martinovic, G.R. Mortier, M.-J. Perez, J. Roume, G. Scarano, A.
740 Munnich, and V. Cormier-Daire. 2012. NEK1 and DYNC2H1 are both involved in short rib
741 polydactyly Majewski type but not in Beemer Langer cases. *J. Med. Genet.* 49:227-233.

742 Engel, B.D., H. Ishikawa, K.A. Wemmer, S. Geimer, K.I. Wakabayashi, M. Hirono, B. Craige, G.J.
743 Pazour, G.B. Witman, R. Kamiya, and W.F. Marshall. 2012. The role of retrograde
744 intraflagellar transport in flagellar assembly, maintenance, and function. *J. Cell Biol.* 199:151-
745 167.

746 Fan, L., S. Pellegrin, A. Scott, and H. Mellor. 2010. The small GTPase Rif is an alternative trigger for
747 the formation of actin stress fibers in epithelial cells. *J Cell Sci*. 123:1247-1252.

748 Follit, J.A., R.A. Tuft, K.E. Fogarty, and G.J. Pazour. 2006. The intraflagellar transport protein IFT20 is
749 associated with the Golgi complex and is required for cilia assembly. *Mol Biol Cell*. 17:3781-
750 3792.

751 Garcia-Gonzalo, F.R., K.C. Corbit, M.S. Sirerol-Piquer, G. Ramaswami, E.A. Otto, T.R. Noriega, A.D.
752 Seol, J.F. Robinson, C.L. Bennett, D.J. Josifova, J.M. Garcia-Verdugo, N. Katsanis, F.
753 Hildebrandt, and J.F. Reiter. 2011. A transition zone complex regulates mammalian
754 ciliogenesis and ciliary membrane composition. *Nat Genet*. 43:776-784.

755 Garcia-Gonzalo, F.R., and J.F. Reiter. 2017. Open Sesame: How Transition Fibers and the Transition
756 Zone Control Ciliary Composition. *Cold Spring Harb Perspect Biol*. 9.

757 Goetz, S.C., and K.V. Anderson. 2010. The primary cilium: a signalling centre during vertebrate
758 development. *Nat Rev Genet*. 11:331-344.

759 Goggolidou, P., J.L. Stevens, F. Agueci, J. Keynton, G. Wheway, D.T. Grimes, S.H. Patel, H. Hilton, S.K.
760 Morthorst, A. DiPaolo, D.J. Williams, J. Sanderson, S.V. Khoronenkova, N. Powles-Glover, A.
761 Ermakov, C.T. Esapa, R. Romero, G.L. Dianov, J. Briscoe, C.A. Johnson, L.B. Pedersen, and D.P.
762 Norris. 2014. ATMIN is a transcriptional regulator of both lung morphogenesis and
763 ciliogenesis. *Development*. 141:3966-3977.

764 He, M., S. Agbu, and K.V. Anderson. 2017. Microtubule Motors Drive Hedgehog Signaling in Primary
765 Cilia. *Trends in Cell Biology*. 27:110-125.

766 Hou, Y., and G.B. Witman. 2015. Dynein and intraflagellar transport. *Exp. Cell Res.* 334:26-34.

767 Hsu, P.D., E.S. Lander, and F. Zhang. 2014. Development and Applications of CRISPR-Cas9 for
768 Genome Engineering. *Cell*. 157:1262-1278.

769 Hua, K., and R.J. Ferland. 2017. Fixation methods can differentially affect ciliary protein
770 immunolabeling. *Cilia*. 6:5.

771 Huber, C., and V. Cormier-Daire. 2012. Ciliary disorder of the skeleton. *Am J Med Genet C Semin Med*
772 *Genet*. 160C:165-174.

773 Huber, C., S. Wu, A.S. Kim, S. Sigaudy, A. Sarukhanov, V. Serre, G. Baujat, K.H. Le Quan Sang, D.L.
774 Rimoin, D.H. Cohn, A. Munnich, D. Krakow, and V. Cormier-Daire. 2013. WDR34 Mutations
775 that Cause Short-Rib Polydactyly Syndrome Type III/Severe Asphyxiating Thoracic Dysplasia
776 Reveal a Role for the NF-kappaB Pathway in Cilia. *Am. J. Hum. Genet.* 93:926-931.

777 Jensen, V.L., and M.R. Leroux. 2017. Gates for soluble and membrane proteins, and two trafficking
778 systems (IFT and LIFT), establish a dynamic ciliary signaling compartment. *Curr. Opin. Cell*
779 *Biol.* 47:83-91.

780 Kessler, K., I. Wunderlich, S. Uebe, N.S. Falk, A. Giessl, J.H. Brandstatter, B. Popp, P. Klinger, A.B.
781 Ekici, H. Sticht, H.G. Dorr, A. Reis, R. Roepman, E. Seemanova, and C.T. Thiel. 2015. DYNC2LI1
782 mutations broaden the clinical spectrum of dynein-2 defects. *Sci Rep*. 5:11649.

783 Labun, K., T.G. Montague, J.A. Gagnon, S.B. Thyme, and E. Valen. 2016. CHOPCHOP v2: a web tool for
784 the next generation of CRISPR genome engineering. *Nucleic Acids Res.* 44:W272-W276.

785 Larkins, C.E., G.D. Aviles, M.P. East, R.A. Kahn, and T. Caspary. 2011. Arl13b regulates ciliogenesis
786 and the dynamic localization of Shh signaling proteins. *Mol Biol Cell*. 22:4694-4703.

787 Li, A., M. Saito, J.Z. Chuang, Y.Y. Tseng, C. Dedesma, K. Tomizawa, T. Kaitsuka, and C.H. Sung. 2011.
788 Ciliary transition zone activation of phosphorylated Tctex-1 controls ciliary resorption, S-
789 phase entry and fate of neural progenitors. *Nat. Cell Biol.*

790 Li, W., P. Yi, and G. Ou. 2015. Somatic CRISPR–Cas9-induced mutations reveal roles of embryonically
791 essential dynein chains in Caenorhabditis elegans cilia. *The Journal of Cell Biology*. 208:683-
792 692.

793 Liem, K.F., Jr., A. Ashe, M. He, P. Satir, J. Moran, D. Beier, C. Wicking, and K.V. Anderson. 2012. The
794 IFT-A complex regulates Shh signaling through cilia structure and membrane protein
795 trafficking. *The Journal of cell biology*. 197:789-800.

796 May, S.R., A.M. Ashique, M. Karlen, B. Wang, Y. Shen, K. Zarbalis, J. Reiter, J. Ericson, and A.S.
797 Peterson. 2005. Loss of the retrograde motor for IFT disrupts localization of Smo to cilia and
798 prevents the expression of both activator and repressor functions of Gli. *Dev. Biol.* 287:378-
799 389.

800 McInerney-Leo, A.M., M. Schmidts, C.R. Cortes, P.J. Leo, B. Gener, A.D. Courtney, B. Gardiner, J.A.
801 Harris, Y. Lu, M. Marshall, U.K. Consortium, P.J. Scambler, P.L. Beales, M.A. Brown, A. Zankl,
802 H.M. Mitchison, E.L. Duncan, and C. Wicking. 2013. Short-rib polydactyly and Jeune
803 syndromes are caused by mutations in WDR60. *Am. J. Hum. Genet.* 93:515-523.

804 Mei, L., Y. Huang, Q. Pan, W. Su, Y. Quan, D. Liang, and L. Wu. 2015. Targeted next-generation
805 sequencing identifies novel compound heterozygous mutations of DYNC2H1 in a fetus with
806 short rib-polydactyly syndrome, type III. *Clinica chimica acta; international journal of clinical*
807 *chemistry*. 447:47-51.

808 Merrill, A.E., B. Merriman, C. Farrington-Rock, N. Camacho, E.T. Sebald, V.A. Funari, M.J. Schibler,
809 M.H. Firestein, Z.A. Cohn, M.A. Priore, A.K. Thompson, D.L. Rimoin, S.F. Nelson, D.H. Cohn,
810 and D. Krakow. 2009. Ciliary Abnormalities Due to Defects in the Retrograde Transport
811 Protein DYNC2H1 in Short-Rib Polydactyly Syndrome. *Am. J. Hum. Genet.* 84:542-549.

812 Mijalkovic, J., B. Prevo, F. Oswald, P. Mangeol, and E.J.G. Peterman. 2017. Ensemble and single-
813 molecule dynamics of IFT dynein in Caenorhabditis elegans cilia. *Nat Commun*. 8:14591.

814 Mikami, A., S.H. Tynan, T. Hama, K. Luby-Phelps, T. Saito, J.E. Crandall, J.C. Besharse, and R.B. Vallee.
815 2002. Molecular structure of cytoplasmic dynein 2 and its distribution in neuronal and
816 ciliated cells. *J. Cell Sci.* 115:4801-4808.

817 Ocbina, P.J., J.T. Eggenschwiler, I. Moskowitz, and K.V. Anderson. 2011. Complex interactions
818 between genes controlling trafficking in primary cilia. *Nat. Genet.* 43:547-553.

819 Okamoto, T., K. Nagaya, Y. Kawata, H. Asai, E. Tsuchida, F. Nohara, K. Okajima, and H. Azuma. 2015.
820 Novel compound heterozygous mutations in DYNC2H1 in a patient with severe short-rib
821 polydactyly syndrome type III phenotype. *Congenital Anomalies*. 55:155-157.

822 Patel-King, R.S., R.M. Gilberti, E.F.Y. Hom, and S.M. King. 2013. WD60/FAP163 is a dynein
823 intermediate chain required for retrograde intraflagellar transport in cilia. *Mol. Biol. Cell*.
824 24:2668-2677.

825 Pedersen, L.B., S. Geimer, and J.L. Rosenbaum. 2006. Dissecting the molecular mechanisms of
826 intraflagellar transport in Chlamydomonas. *Curr. Biol.* 16:450-459.

827 Prevo, B., P. Mangeol, F. Oswald, J.M. Scholey, and E.J. Peterman. 2015. Functional differentiation of
828 cooperating kinesin-2 motors orchestrates cargo import and transport in C. elegans cilia.
829 *Nat. Cell Biol.* 17:1536-1545.

830 Reck, J., A.M. Schauer, K. VanderWaal Mills, R. Bower, D. Tritschler, C.A. Perrone, and M.E. Porter.
831 2016. The role of the dynein light intermediate chain in retrograde IFT and flagellar function
832 in Chlamydomonas. *Mol. Biol. Cell*. 27:2404-2422.

833 Reiter, J.F., and M.R. Leroux. 2017. Genes and molecular pathways underpinning ciliopathies. *Nat*
834 *Rev Mol Cell Biol*. 18:533-547.

835 Roberts, A.J., T. Kon, P.J. Knight, K. Sutoh, and S.A. Burgess. 2013. Functions and mechanics of dynein
836 motor proteins. *Nature reviews. Molecular cell biology*. 14:713-726.

837 Rompolas, P., L.B. Pedersen, R.S. Patel-King, and S.M. King. 2007. Chlamydomonas FAP133 is a
838 dynein intermediate chain associated with the retrograde intraflagellar transport motor. *J.*
839 *Cell Sci.* 120:3653-3665.

840 Schmidts, M., H.H. Arts, E.M. Bongers, Z. Yap, M.M. Oud, D. Antony, L. Duijkers, R.D. Emes, J. Stalker,
841 J.B. Yntema, V. Plagnol, A. Hoischen, C. Gilissen, E. Forsythe, E. Lausch, J.A. Veltman, N.
842 Roeleveld, A. Superti-Furga, A. Kutkowska-Kazmierczak, E.J. Kamsteeg, N. Elcioglu, M.C. van
843 Maarle, L.M. Graul-Neumann, K. Devriendt, S.F. Smithson, D. Wellesley, N.E. Verbeek, R.C.
844 Hennekam, H. Kayserili, P.J. Scambler, P.L. Beales, N.V. Knoers, R. Roepman, and H.M.
845 Mitchison. 2013a. Exome sequencing identifies DYNC2H1 mutations as a common cause of
846 asphyxiating thoracic dystrophy (Jeune syndrome) without major polydactyly, renal or
847 retinal involvement. *J. Med. Genet.* 50:309-323.

848 Schmidts, M., Y. Hou, C.R. Cortes, D.A. Mans, C. Huber, K. Boldt, M. Patel, J. van Reeuwijk, J.M. Plaza,
849 S.E. van Beersum, Z.M. Yap, S.J. Letteboer, S.P. Taylor, W. Herridge, C.A. Johnson, P.J.
850 Scambler, M. Ueffing, H. Kayserili, D. Krakow, S.M. King, P.L. Beales, L. Al-Gazali, C. Wicking,
851 V. Cormier-Daire, R. Roepman, H.M. Mitchison, G.B. Witman, and Uk10K. 2015. TCTEX1D2
852 mutations underlie Jeune asphyxiating thoracic dystrophy with impaired retrograde
853 intraflagellar transport. *Nat Commun*. 6:7074.

854 Schmidts, M., J. Vodopiutz, S. Christou-Savina, C.R. Cortés, A.M. McInerney-Leo, R.D. Emes, H.H.
855 Arts, B. Tüysüz, J. D'Silva, P.J. Leo, T.C. Giles, M.M. Oud, J.A. Harris, M. Koopmans, M.
856 Marshall, N. Elçioglu, A. Kuechler, D. Bockenhauer, A.T. Moore, L.C. Wilson, A.R. Janecke,
857 M.E. Hurles, W. Emmet, B. Gardiner, B. Streubel, B. Dopita, A. Zankl, H. Kayserili, P.J.
858 Scambler, M.A. Brown, P.L. Beales, C. Wicking, UK10K, E.L. Duncan, and H.M. Mitchison.
859 2013b. Mutations in the gene encoding IFT dynein complex component WDR34 cause Jeune
860 asphyxiating thoracic dystrophy. *Am. J. Hum. Genet.* 93:932-944.

861 Shi, X., G. Garcia, 3rd, J.C. Van De Weghe, R. McGorty, G.J. Pazour, D. Doherty, B. Huang, and J.F.
862 Reiter. 2017. Super-resolution microscopy reveals that disruption of ciliary transition-zone
863 architecture causes Joubert syndrome. *Nat. Cell Biol.* 19:1178-1188.

864 Signor, D., K.P. Wedaman, J.T. Orozco, N.D. Dwyer, C.I. Bargmann, L.S. Rose, and J.M. Scholey. 1999.
865 Role of a class DHC1b dynein in retrograde transport of IFT motors and IFT raft particles
866 along cilia, but not dendrites, in chemosensory neurons of living Caenorhabditis elegans. *J.*
867 *Cell Biol.* 147:519-530.

868 Taipale, M., G. Tucker, J. Peng, I. Krykbaeva, Z.Y. Lin, B. Larsen, H. Choi, B. Berger, A.C. Gingras, and S.
869 Lindquist. 2014. A quantitative chaperone interaction network reveals the architecture of
870 cellular protein homeostasis pathways. *Cell*. 158:434-448.

871 Taylor, S.P., T.J. Dantas, I. Duran, S. Wu, R.S. Lachman, M.J. Bamshad, J. Shendure, D.a. Nickerson,
872 S.F. Nelson, D.H. Cohn, R.B. Vallee, and D. Krakow. 2015. Mutations in DYNC2LI1 disrupt cilia
873 function and cause short rib polydactyly syndrome. *Nat Commun*. 6:7092.

874 Toropova, K., M. Mladenov, and A.J. Roberts. 2017. Intraflagellar transport dynein is autoinhibited
875 by trapping of its mechanical and track-binding elements. *Nat Struct Mol Biol*. 24:461-468.

876 Williams, C.L., J.C. McIntyre, S.R. Norris, P.M. Jenkins, L. Zhang, Q. Pei, K. Verhey, and J.R. Martens.
877 2014. Direct evidence for BBSome-associated intraflagellar transport reveals distinct
878 properties of native mammalian cilia. *Nat Commun*. 5:5813.

879 Williamson, S.M., D.A. Silva, E. Richey, and H. Qin. 2012. Probing the role of IFT particle complex A
880 and B in flagellar entry and exit of IFT-dynein in Chlamydomonas. *Protoplasma*. 249:851-856.

881 Wu, C., J. Li, A. Peterson, K. Tao, and B. Wang. 2017. Loss of dynein-2 intermediate chain Wdr34
882 results in defects in retrograde ciliary protein trafficking and Hedgehog signaling in the
883 mouse. *Hum Mol Genet*. 26:2386-2397.

884 Yee, L.E., and J.F. Reiter. 2015. Ciliary vesicle formation: a prelude to ciliogenesis. *Dev. Cell*. 32:665-
885 666.

886 Yi, P., W.J. Li, M.Q. Dong, and G. Ou. 2017. Dynein-Driven Retrograde Intraflagellar Transport Is
887 Triphasic in C. elegans Sensory Cilia. *Curr. Biol.* 27:1448-1461 e1447.

888

Figure 1

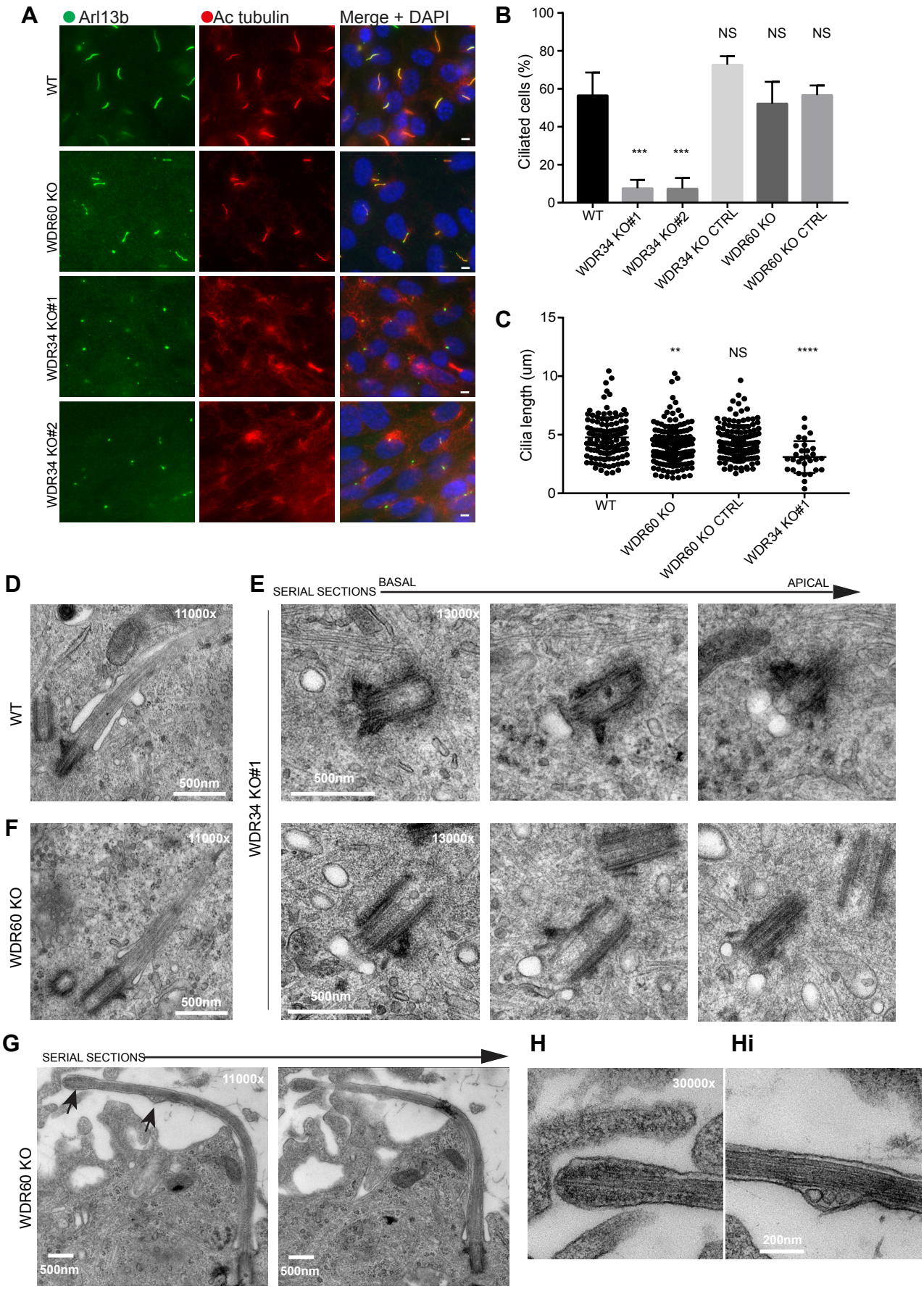
A
Arl13b
Ac tubulin
Merge + DAPI
WT
WDR60 KO
WDR34 KO#1
WDR34 KO#2
B
Ciliated cells (%)
100
80
60
40
20
0
***
***
NS
NS
NS
WT
WDR34 KO#1
WDR34 KO#2
WDR34 KO CTRL
WDR60 KO
WDR60 KO CTRL
C
Cilia length (um)
15
10
5
0
**
NS
****
WT
WDR60 KO
WDR60 KO CTRL
WDR34 KO#1
D
WT
11000x
500nm
E
SERIAL SECTIONS
BASAL
APICAL
WDR34 KO#1
13000x
500nm
F
WDR60 KO
11000x
500nm
13000x
500nm
G
SERIAL SECTIONS
WDR60 KO
11000x
500nm
500nm
H
30000x
Hi
200nm

Figure 2

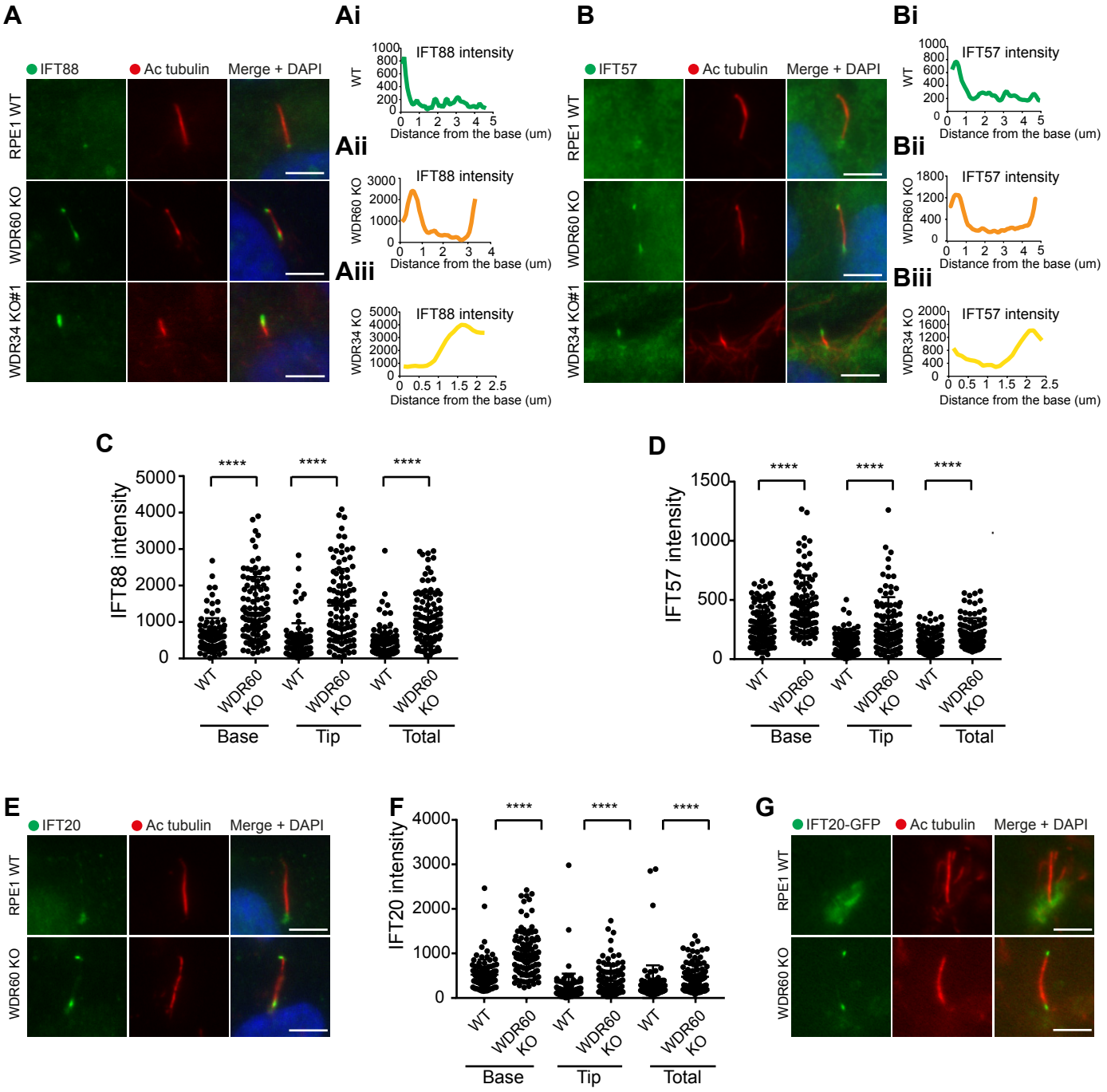
A
IFT88
Ac tubulin
Merge + DAPI
RPE1 WT
WDR60 KO
WDR34 KO#1
Ai
Aii
Aiii
IFT88 intensity
Distance from the base (um)
B
IFT57
Bi
Bii
Biii
IFT57 intensity
C
IFT88 intensity
****
WT
WDR60 KO
Base
Tip
Total
D
IFT57 intensity
E
IFT20
F
IFT20 intensity
G
IFT20-GFP

Figure 3

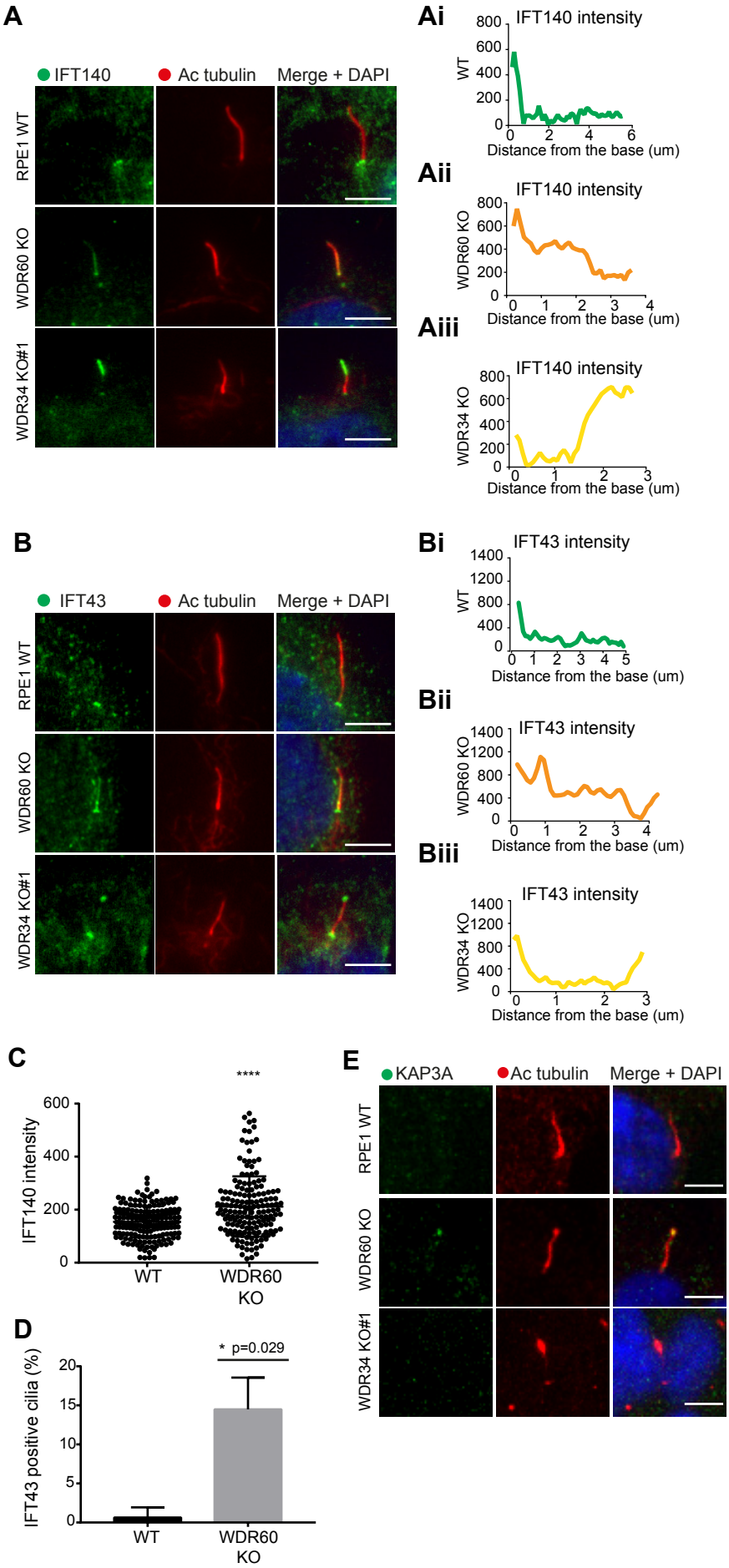
A
IFT140
Ac tubulin
Merge + DAPI
RPE1 WT
WDR60 KO
WDR34 KO#1
Ai
IFT140 intensity
WT
Distance from the base (um)
Aii
IFT140 intensity
WDR60 KO
Distance from the base (um)
Aiii
IFT140 intensity
WDR34 KO
Distance from the base (um)
B
IFT43
Ac tubulin
Merge + DAPI
RPE1 WT
WDR60 KO
WDR34 KO#1
Bi
IFT43 intensity
WT
Distance from the base (um)
Bii
IFT43 intensity
WDR60 KO
Distance from the base (um)
Biii
IFT43 intensity
WDR34 KO
Distance from the base (um)
C
IFT140 intensity
****
WT
WDR60 KO
D
IFT43 positive cilia (%)
* p=0.029
WT
WDR60 KO
E
KAP3A
Ac tubulin
Merge + DAPI
RPE1 WT
WDR60 KO
WDR34 KO#1

Figure 4

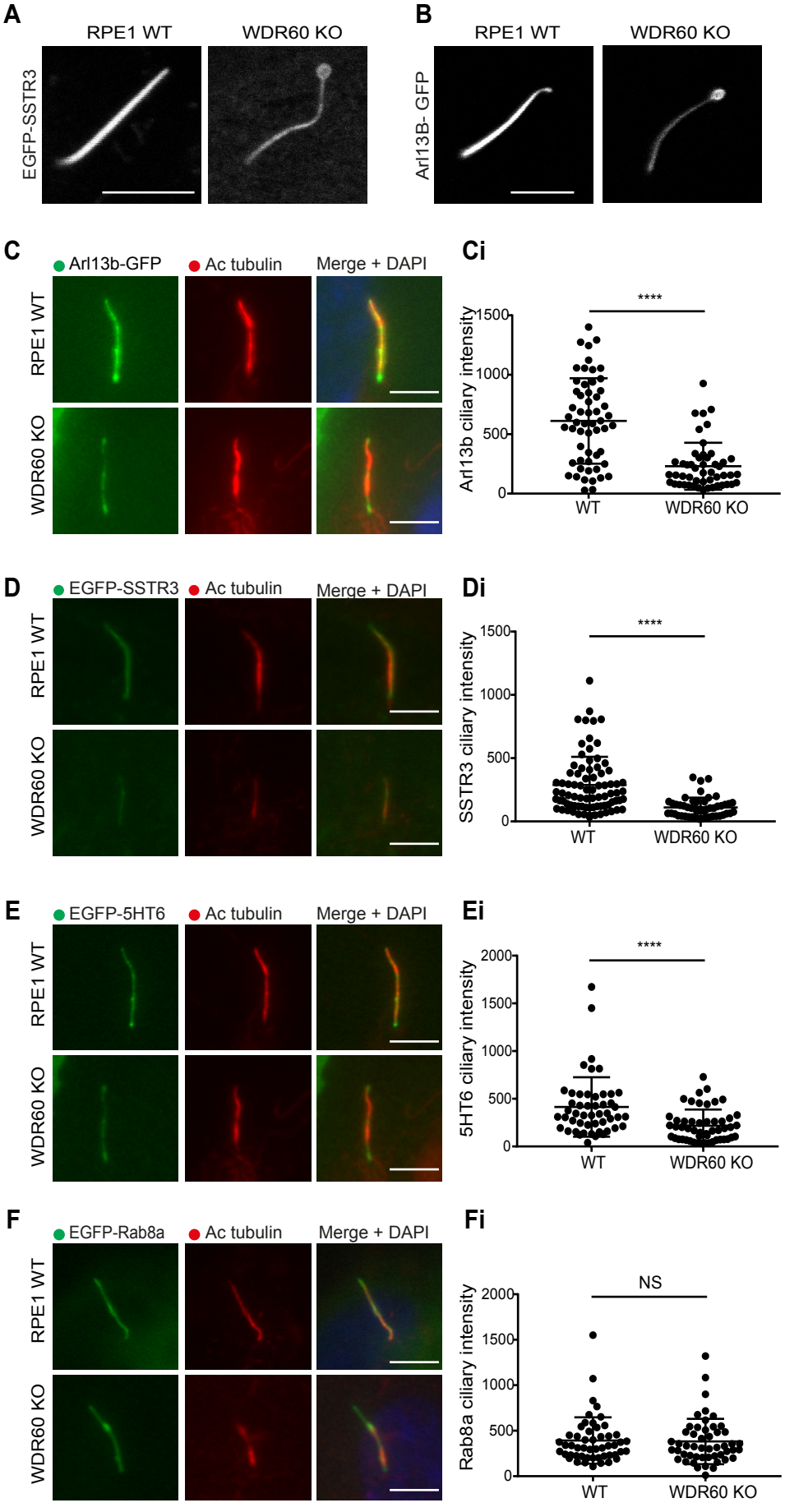
A
RPE1 WT
WDR60 KO
EGFP-SSTR3
B
RPE1 WT
WDR60 KO
Arl13B- GFP
C
Arl13b-GFP
Ac tubulin
Merge + DAPI
RPE1 WT
WDR60 KO
Ci
Arl13b ciliary intensity
1500
1000
500
0
****
WT
WDR60 KO
D
EGFP-SSTR3
Ac tubulin
Merge + DAPI
RPE1 WT
WDR60 KO
Di
SSTR3 ciliary intensity
1500
1000
500
0
****
WT
WDR60 KO
E
EGFP-5HT6
Ac tubulin
Merge + DAPI
RPE1 WT
WDR60 KO
Ei
5HT6 ciliary intensity
2000
1500
1000
500
0
****
WT
WDR60 KO
F
EGFP-Rab8a
Ac tubulin
Merge + DAPI
RPE1 WT
WDR60 KO
Fi
Rab8a ciliary intensity
2000
1500
1000
500
0
NS
WT
WDR60 KO

Figure 5

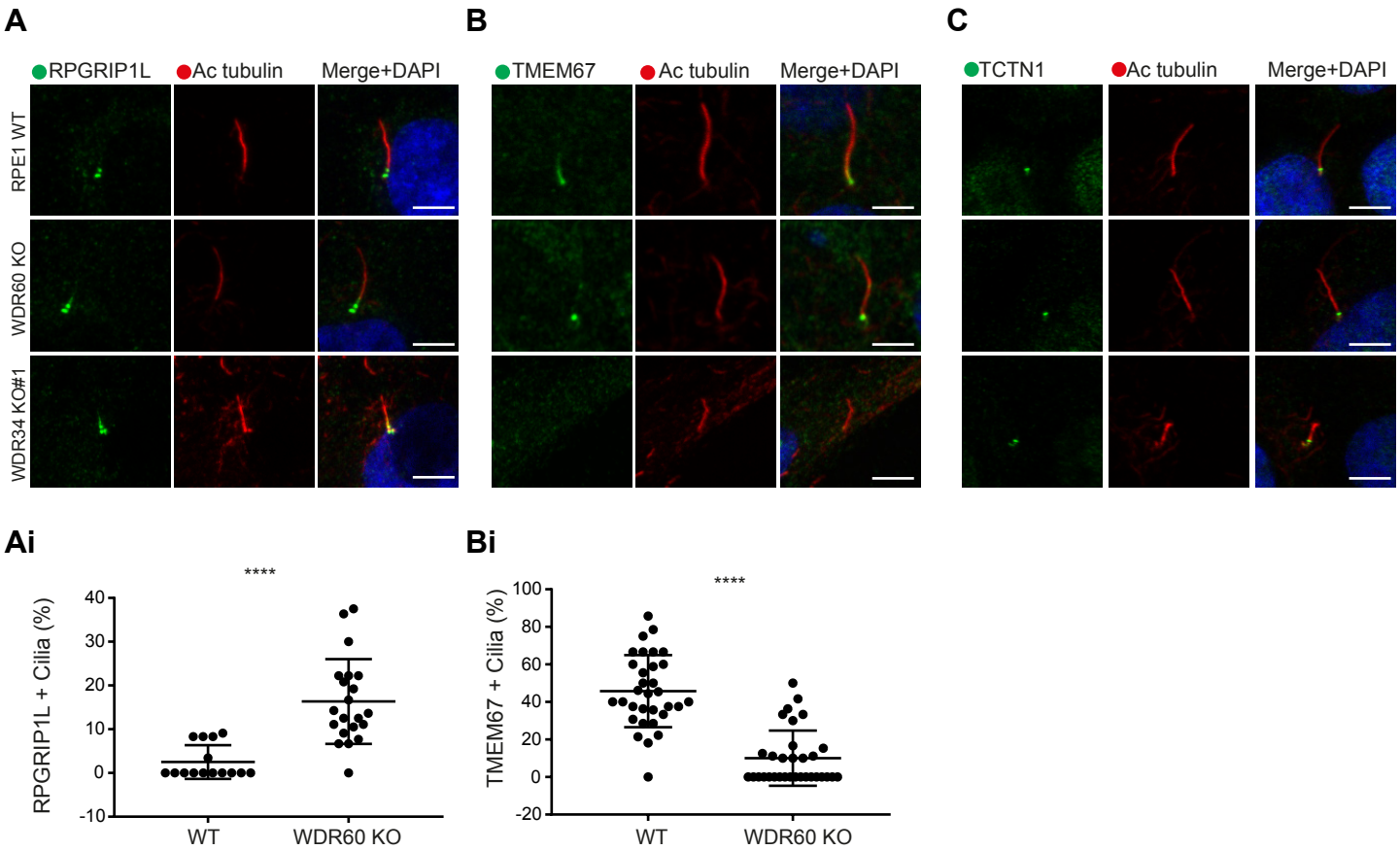
A
RPGRIP1L
Ac tubulin
Merge+DAPI
RPE1 WT
WDR60 KO
WDR34 KO#1
B
TMEM67
Ac tubulin
Merge+DAPI
C
TCTN1
Ac tubulin
Merge+DAPI
Ai
RPGRIP1L + Cilia (%)
****
40
30
20
10
0
-10
WT
WDR60 KO
Bi
TMEM67 + Cilia (%)
****
100
80
60
40
20
0
-20
WT
WDR60 KO

Figure 6

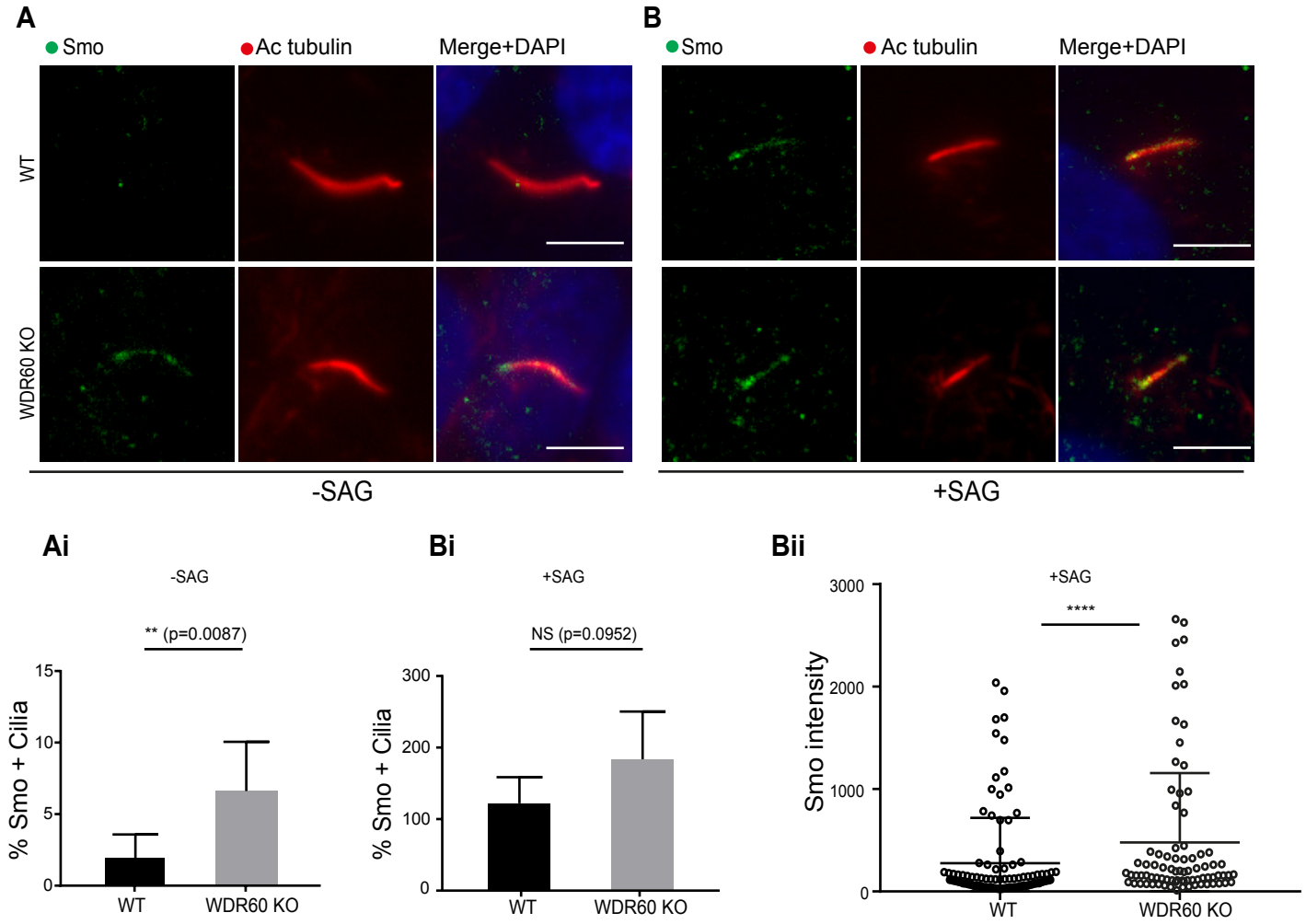
A
Smo
Ac tubulin
Merge+DAPI
WT
WDR60 KO
-SAG
B
Smo
Ac tubulin
Merge+DAPI
+SAG
Ai
-SAG
** (p=0.0087)
% Smo + Cilia
15
10
5
0
WT
WDR60 KO
Bi
+SAG
NS (p=0.0952)
% Smo + Cilia
300
200
100
0
WT
WDR60 KO
Bii
+SAG
****
Smo intensity
3000
2000
1000
0
WT
WDR60 KO

Figure 7

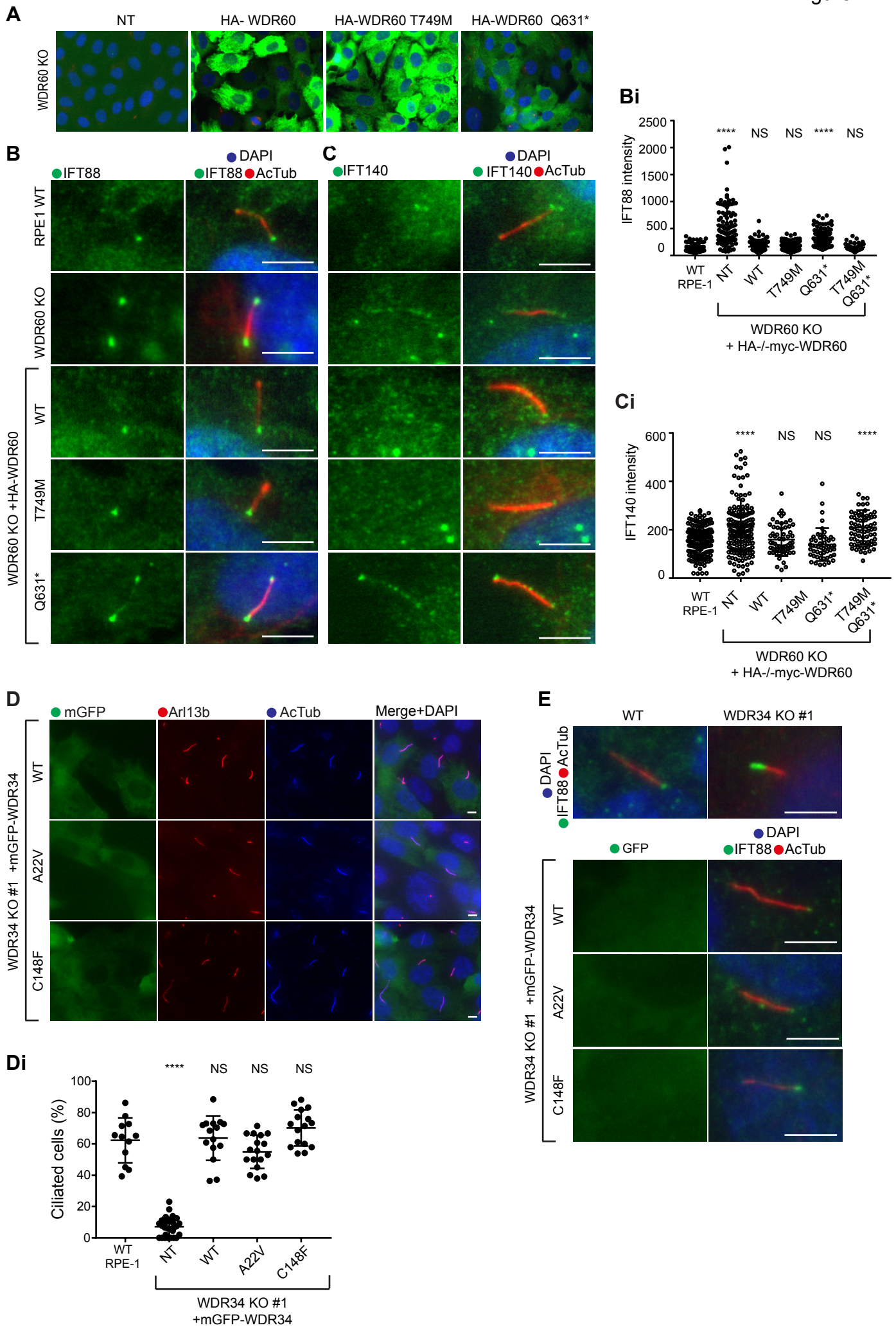
A
NT
HA- WDR60
HA-WDR60 T749M
HA-WDR60 Q631*
WDR60 KO
B
IFT88
DAPI
IFT88 AcTub
RPE1 WT
WDR60 KO
WDR60 KO +HA-WDR60
WT
T749M
Q631*
C
IFT140
DAPI
IFT140 AcTub
Bi
IFT88 intensity
2500
2000
1500
1000
500
0
****
NS
NS
****
NS
WT RPE-1
NT
WT
T749M
Q631*
T749M Q631*
WDR60 KO
+ HA-/-myc-WDR60
Ci
IFT140 intensity
600
400
200
0
****
NS
NS
****
WT RPE-1
NT
WT
T749M
Q631*
T749M Q631*
WDR60 KO
+ HA-/-myc-WDR60
D
mGFP
Arl13b
AcTub
Merge+DAPI
WDR34 KO #1 +mGFP-WDR34
WT
A22V
C148F
Di
Ciliated cells (%)
100
80
60
40
20
0
****
NS
NS
NS
WT RPE-1
NT
WT
A22V
C148F
WDR34 KO #1
+mGFP-WDR34
E
WT
WDR34 KO #1
DAPI
IFT88 AcTub
GFP
DAPI
IFT88 AcTub
WDR34 KO #1 +mGFP-WDR34
WT
A22V
C148F

Figure 8

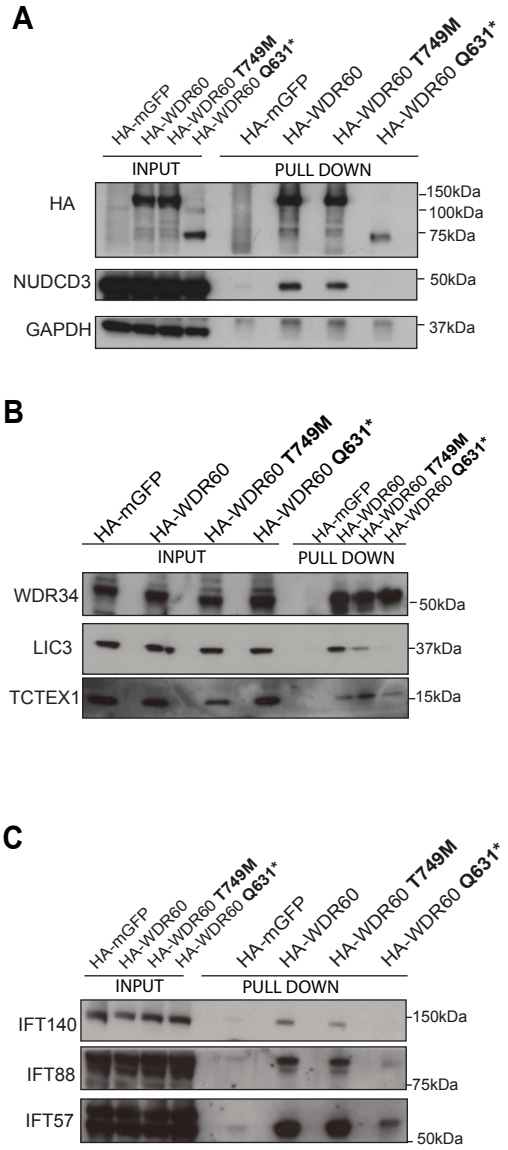
A
HA-mGFP
HA-WDR60
HA-WDR60 T749M
HA-WDR60 Q631*
HA-mGFP
HA-WDR60
HA-WDR60 T749M
HA-WDR60 Q631*
INPUT
PULL DOWN
HA
NUDCD3
GAPDH
150kDa
100kDa
75kDa
50kDa
37kDa
B
HA-mGFP
HA-WDR60
HA-WDR60 T749M
HA-WDR60 Q631*
HA-mGFP
HA-WDR60
HA-WDR60 T749M
HA-WDR60 Q631*
INPUT
PULL DOWN
WDR34
LIC3
TCTEX1
50kDa
37kDa
15kDa
C
HA-mGFP
HA-WDR60
HA-WDR60 T749M
HA-WDR60 Q631*
HA-mGFP
HA-WDR60
HA-WDR60 T749M
HA-WDR60 Q631*
INPUT
PULL DOWN
IFT140
IFT88
IFT57
150kDa
75kDa
50kDa

Figure 9

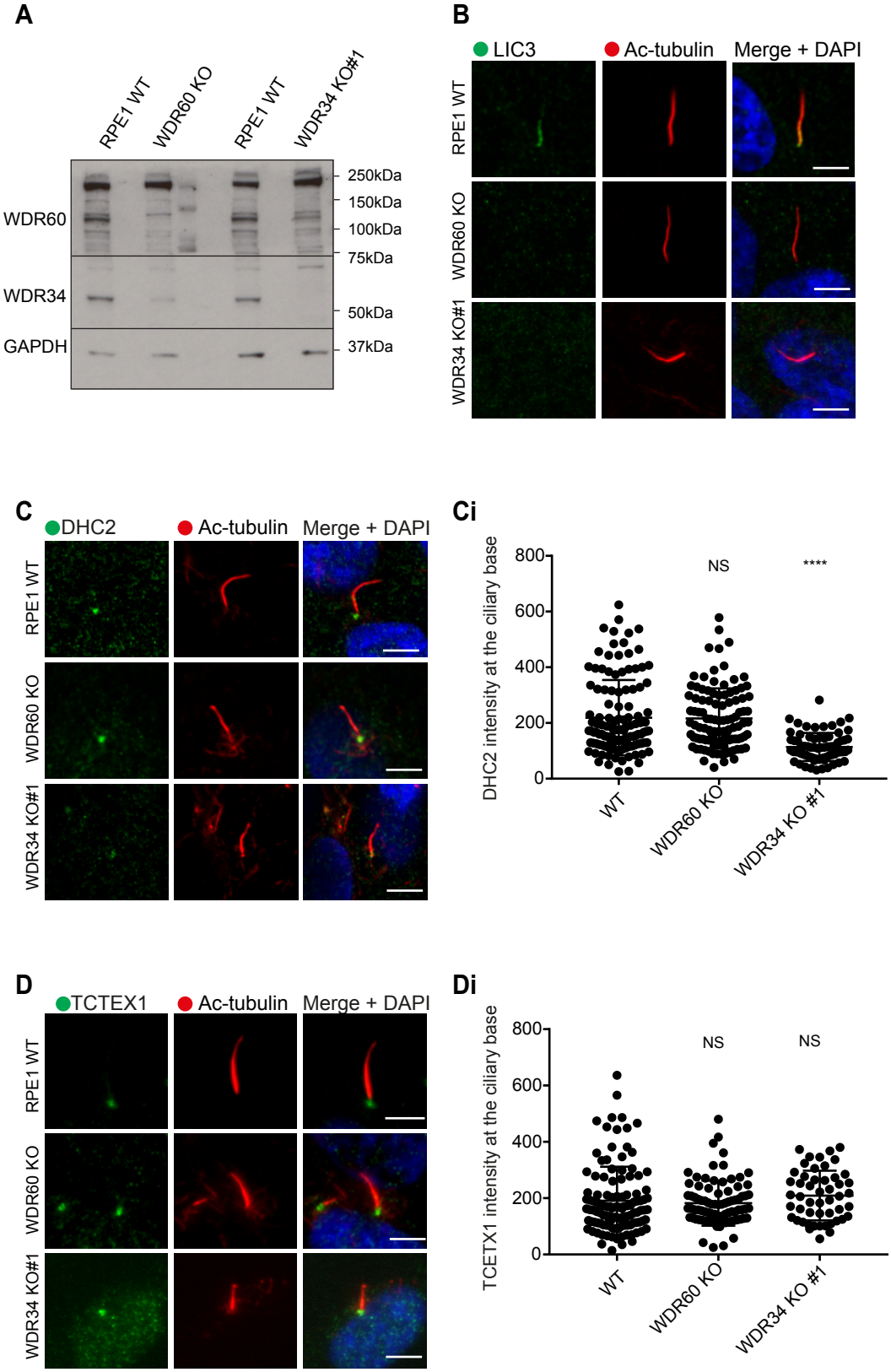
A
RPE1 WT
WDR60 KO
RPE1 WT
WDR34 KO#1
WDR60
WDR34
GAPDH
250kDa
150kDa
100kDa
75kDa
50kDa
37kDa
B
LIC3
Ac-tubulin
Merge + DAPI
RPE1 WT
WDR60 KO
WDR34 KO#1
C
DHC2
Ac-tubulin
Merge + DAPI
RPE1 WT
WDR60 KO
WDR34 KO#1
Ci
DHC2 intensity at the ciliary base
800
600
400
200
0
NS
****
WT
WDR60 KO
WDR34 KO #1
D
TCTEX1
Ac-tubulin
Merge + DAPI
RPE1 WT
WDR60 KO
WDR34 KO#1
Di
TCETX1 intensity at the ciliary base
800
600
400
200
0
NS
NS
WT
WDR60 KO
WDR34 KO #1

Figure 10

A

Gene ID	**HA-WDR34** (WT)/(WDR60 KO)	**HA-WDR60** (WT)/(WDR34 KO#1)
DYNC2H1	10.9	1.6
WDR60		0.8
WDR34	1.1	
DYNC2LI1	2.6	1.0
DYNLT1	9.4	0.8
TCTEX1D2	2.8	0.8
DYNLT3	2.1	1.7
DYNLL1	1.6	1.1
DYNLL2	1.6	1.2
DYNLRB1	1.7	2.5
NUDC	2.2	0.9
NUDCD3	2.4	1.1
IFT54	1.6	0.8
IFT57	2.3	1.3
IFT74	2.5	1.2
IFT88	2.3	1.4
IFT172	1.7	1.0
BBS7	1.5	0.7
BBS9	1.7	1.0

B

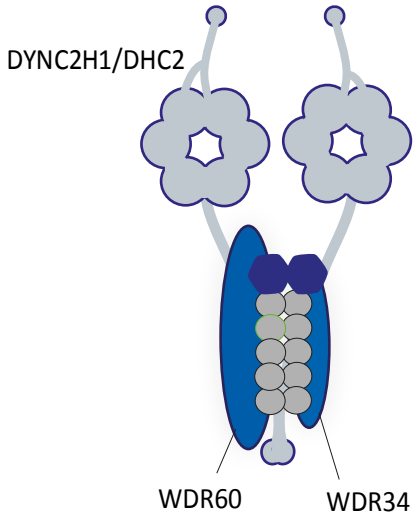

WT

Bi

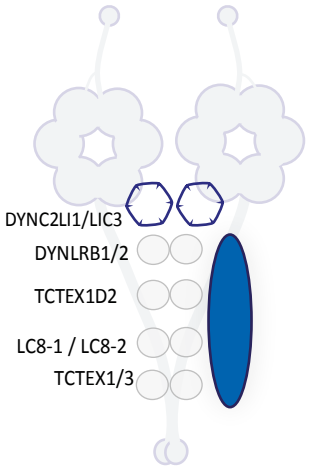

WDR60 KO

Bii

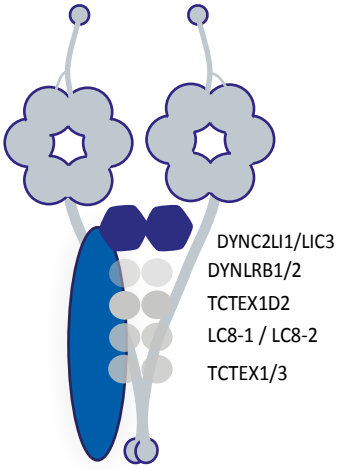

WDR34 KO